information services
gwasanaethau gwybodaeth

# The simulation of crack opening–closing and aggregate interlock behaviour in finite element concrete models

**A. D. Jefferson\*  and  I. C. Mihai**

Cardiff University, School of Engineering, Queen's Buildings, The Parade CF24 3AA, UK

\* Corresponding author. E-mail address: JeffersonAD@cf.ac.uk

Tel: +44 (0) 2920 875697

**ABSTRACT**

The ability to  model crack closure behaviour and aggregate interlock in finite element concrete models is extremely important. Both of these phenomena arise from the same contact mechanisms and the advantages of modelling them in a unified manner are highlighted. An example illustrating the numerical difficulties that arise when abrupt crack closure is modelled is presented and the benefits of smoothing this behaviour are discussed. We present a new crack-plane model that uses an effective contact surface derived directly from experimental data and which is described by a signed-distance function in relative-displacement space. The introduction of a crack-closure transition function into the formulation improves its accuracy and enhances its robustness. The characteristic behaviour of the new smoothed crack-plane model is illustrated for a series of relative-displacement paths. We describe a method for incorporating the model into continuum elements using a crack band approach and address a previously overlooked issue associated with scaling the inelastic shear response of a crack-band. A consistent algorithmic tangent and associated stress recovery procedure are derived.  Finally, a series of examples are presented demonstrating that the new model is able to represent a range of cracked concrete behaviour with good accuracy and robustness.

# 1. INTRODUCTION

Nearly all reinforced concrete structures contain cracks and most of these structures are subject to a degree of variable loading which causes cracks to open and close. In the most extreme situations, such as during earthquakes, structures are subject to multiple loading/unloading cycles, which result in cracks opening and closing many times [1-3]. Even under monotonic loading, a certain percentage of cracks open and then close again as other cracks become dominant [4]. The opposing surfaces of these cracks contain multiple asperities which can come into contact under combinations of shear and opening displacements even when a crack has a significant opening. When this type of rough crack shear contact occurs in concrete it is commonly described as 'aggregate interlock' [5-6] and this is an important load carrying mechanism that accounts for 35–50% of the ultimate load carrying capacity of some reinforced concrete structural elements [5]. The opening–closing and contact behaviour of rough cracks are thus key characteristics of concrete that should be considered in finite element concrete models. However, the introduction of crack contact into a concrete constitutive model can give rise to numerical difficulties over and above the much discussed stability and mesh dependency problems associated with simulating cracking, or strain softening, behaviour [7-13]. The numerical difficulties associated with modelling crack opening–closing behaviour have been acknowledged (sometimes implicitly) by various authors [2,8,14,15] but have not received the same level of attention as the aforementioned stability and mesh dependency problems. A particular exception to this was the work of Feenstra et al. [14] who explored the accuracy and stability of a range of rough crack models applied to interface elements. The authors reported that equilibrium convergence was achieved in each analysis but, in some instances, very small load increments were required to achieve this convergence and it was not always possible to use the tangent stiffness matrix. Such difficulties were experienced on relatively small scale problems with a single interface; these difficulties are compounded in situations where multiple interfaces undergo multiple changes in contact state.

The experience of the present authors when using the model described in reference [16] is that numerical breakdown of an incremental-iterative finite element solution occurs more regularly when the crack-closure component is active than when it is inactive which concurs with the anecdotal experience of other researchers. These difficulties are considered an impediment to the use of rough contact models in the analysis of real structures. This paper discusses these issues and proposes a new model that not only addresses these numerical problems but is also more accurate and tractable than that the model described in reference [16].

Before considering previous work on modelling aspects of crack closure and aggregate interlock, it is necessary to outline some important experimental work. Several experimental studies investigated shear transfer mechanisms across formed macro-cracks in reinforced concrete specimens [17-19]. In later studies, mixed mode (shear-normal) fracture behaviour was investigated [20-22]. These latter studies involved tests in which cracks were opened under normal loading and then subjected to various combinations of normal and shear loading, as well as tests in which cracks were both formed and evolved under mixed mode loading. Recently, Jacobsen et al. [23] described some new mixed mode tests on cracked concrete samples. The deeply notched specimens employed in these studies were

1

designed to give 'the mixed mode material point behaviour of a crack in concrete' so as to isolate this behaviour from structural effects and to avoid secondary cracking.

A knowledge of the morphology of crack surfaces in concrete is also important in understanding the associated rough crack contact behaviour and a number of studies have included direct measurements of crack-surface topology [24-26].

Experimental studies on the direct crack opening-closing behaviour of concrete have been undertaken by Reinhardt [27]. In this work, the author explored the response of cracks at varying initial openings for a range of closing stresses.

Crack closure and aggregate interlock were often considered separately in finite element smeared crack models [28-30], with a popular method for approximating the effects of aggregate interlock being to use a 'shear retention factor' on the shear component of a cracked modulus matrix [28-32]. The retention of some shear strength in such models is generally considered to improve their stability [31]. Direct crack closure was simulated in some of these models by recovering the stiffness component normal to the crack surface when the normal stress became compressive [28,30,4]. Particular flaws with shear retention methods include their inability to simulate both the build-up of compressive stresses and the delayed contact that occurs when open cracks undergo shear, both of which are evident in the tests of Walraven and Reinhardt [19].

Stiffness recovery due to crack closure (sometimes referred to as the 'unilateral effect') has been considered in a number of continuum damage and plastic-damage constitutive models [33]. A particular procedure involving the recovery of stiffness in models that decompose the stress and strain tensors into positive and negative parts [34] was shown (under certain circumstances) to lead to thermodynamically inconsistent results [35], but these issues appear to have been resolved in a recent formulation by Wu and Xu [36].

An alternative approach for such models is to use volumetric/deviatoric decompositions of stress/strain tensors and to recover only the volumetric component of stiffness when the mean stress becomes compressive [2,37,38]. This approach has been extended by Richard et al. [15] and Richard and Raganeau [39], who have coupled volumetric stiffness recovery to frictional behaviour on the damaged deviatoric component of the constitutive relationships. Richard et al. [15] identify the volumetric/deviatoric separation of the 'unilateral effect' as 'the key point for an easy identification and a robust numerical implementation'. These continuum damage approaches deal mainly with the effects of micro-crack closure but become inaccurate when rough macro-crack contact behaviour is considered, for which a more direct representation of the macro-crack is required.

A number of constitutive relationships have been developed for rough macro-cracks which relate crack-plane tractions to the relative-displacements between opposing crack faces [6,19,24,40-46]. Of these models, those that are based directly upon the degree of contact between the measured asperities on opposing rough crack surfaces include

2

the contact density formulations of Li et al. [24] and Ali and White [43]; the interacting sphere model of Walraven and Reinhardt [19]; and the rough crack contact model based on cone-shaped asperities of Mihai and Jefferson [46].

A number of cohesive zone plasticity-based models, with and without crack-closure behaviour, have also been developed to represent the behaviour of cracks [26,47-50]. These have, for example, been applied to meso-scale simulations of concrete specimens as well as to interface elements in macroscopic simulations.

The model developed in this paper is classed as a cohesive zone model, an approach pioneered by Hillerborg et al. [51]. This type of model was initially used to govern the constitutive behaviour of finite element interface elements but the approach was later extended in the form of the 'crack band model' and applied to continuum elements [7]. A recent study of various aspects of the crack band approach has been made by Jirasek and Bauer [51]. The new model is applied to a crack plane and aims to represent the development of the fracture process zone as well as the behaviour of a fully formed crack. The model can be applied to embedded crack planes in continuum elements using the smeared crack-band approach [7,52], interface elements [47,50,53], elements with strong discontinuities [54-55] as well as to discontinuities introduced via mesh-based strong discontinuities, or X-FEM [56-58]. Interestingly, Mosler and Meschke [59] showed that in many situations fracture energy based smeared crack models give essentially the same response as elements with strong discontinuities. A rough crack model has been incorporated into an element with strong discontinuity by Theiner and Hofstetter [53] and applied to some real engineering problems, including the pull-out of a steel anchor. Sellier et al. [60] showed the benefits of smoothing crack opening/closing behaviour in their orthotropic damage model and this idea of smoothing the contact behaviour is particularly relevant to the work described in the current paper.

The present authors consider that models that use a split between damaged and undamaged behaviour of a representative crack-plane area, and that include mechanisms for the recovery of a proportion of the damaged stiffness, provide a natural means of simulating the evolution of cracks and crack closure [15,16,39,45,61,62]. We also believe that rough contact models which simulate both direct crack closure and shear contact (or aggregate interlock) behaviour in a unified manner best represent the reality of the contact behaviour that occurs between the rough surfaces of cracks in concrete [16,19,24,43,46].

The aim of the paper is to present a new robust model for simulating concrete cracking that includes crack formation, the evolution of cracks, and rough crack contact behaviour in a unified manner. The particular innovations / new aspects of this work are (i) the identification of a smooth effective contact function, derived directly from experimental data, with the properties of signed distance function; (ii) the introduction of an experimentally calibrated function to provide a transition from a fully closed to a fully open contact state in a completely smooth fashion for crack closure under mode 1 and mixed mode loading conditions; (iii) the presentation of a procedure that addresses mesh dependence in smeared crack models when a shear contact or shear retention procedure is employed; (iv) the derivation of a consistent algorithmic tangent matrix and associated stress recovery procedure for

the model with transition; and (v) a series of finite element analyses that consider experimental tests, in particular, the recent tests of Jacobsen et al. [23].

The layout of the remainder of the paper is as follows:

Section 2   discusses the reasons for convergence difficulties inherent in simulating crack-closure.

Section 3   presents a new rough crack contact model for discrete cracks.

Section 4   presents results for a few selected stress vs  relative-displacement paths to illustrate the characteristic behaviour of the model.

Section 5   shows how the model can be incorporated into continuum finite elements via the crack-band approach, which is extended to incorporate a new form of shear contact scaling. This section also gives the derivations of a consistent algorithmic tangent matrix and stress recovery procedure for the crack-plane model with contact transition.

Section 6   provides a number of examples and a numerical convergence study, which examines the performance of the model with different degrees of closure transition.

Section 7   gives conclusions from the work.

## 2.  THE CHALLENGES OF SIMULATING CRACK OPENING/CLOSING BEHAVIOUR

For the purposes of the present discussion, an idealised cracking problem is considered which is based on the mesh and the material properties given in Figure 1, in which $E$ is Young's modulus, $f_t$ is the tensile strength and $G_f$ is the fracture energy parameter. In this hypothetical problem, a crack is opened in a notched concrete specimen to a crack opening displacement of 0.1mm. At this point a compressive stress of 0.5MPa is applied to the specimen to close the crack. It is assumed that the theoretical unloading response follows a secant path to the origin and then regains the uncracked stiffness in the compressive region.  The authors have observed that this type of crack opening/closing behaviour occurs in multiple locations in full scale finite element analyses of reinforced concrete structures when certain cracks become dominant and other adjacent cracks close.

If a simplified 1D response is considered then, using secant unloading at point A in Figure 2, the relative-displacement at the end of the first iteration after the compressive load is applied would be -0.855mm. If this is translated into a strain over the localised region (i.e. over the height of the central row of elements), the strain value would -0.171. When the crack fully closes, the behaviour reverts to linear elastic, so the uniaxial stress associated with this strain would be  -5130 MPa, if no compressive limit is applied.

The authors have observed that when such behaviour occurs, there is a tendency for solutions to oscillate between open and closed states. Furthermore, these relatively large strains and stresses result in spurious cracking and crushing, with the result that convergence is difficult to obtain. There are techniques to deal with this type of problem [13] but such abrupt changes in response will always be a challenge for nonlinear finite element solution schemes.

One of our aims is to address this problem by developing a new model in which all contact behaviour is smoothed over a contact transition region such that the changes in stresses and strain during contact are far less abrupt than in the example described.

This type of behaviour is akin to the chatter that occurs in contact mechanics, and in such situations smoothing contact penalty functions are sometimes employed [64].
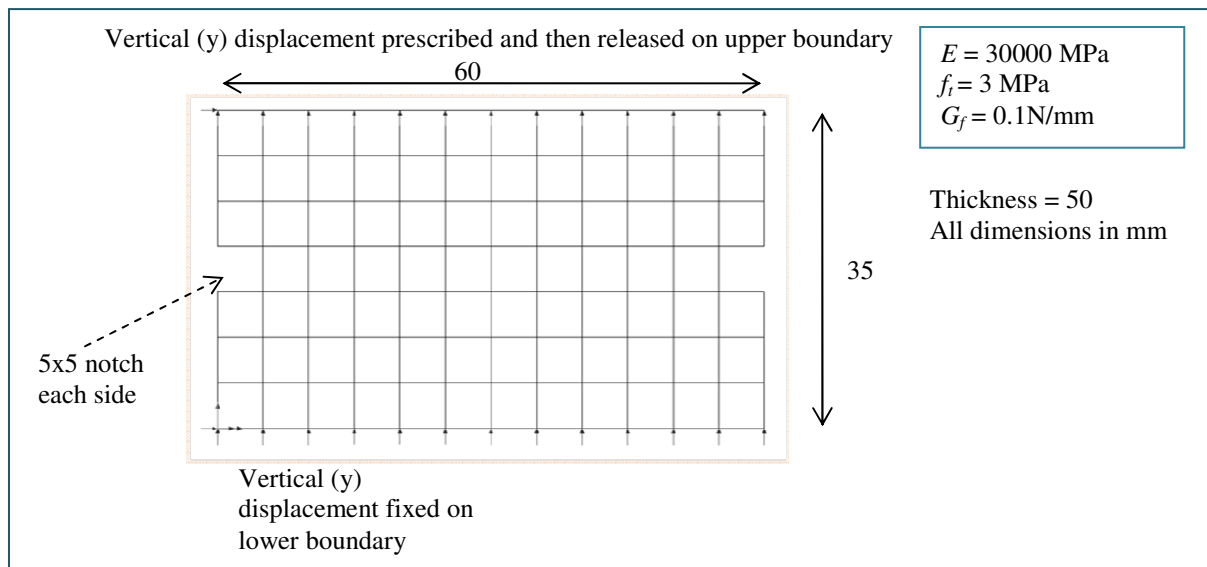


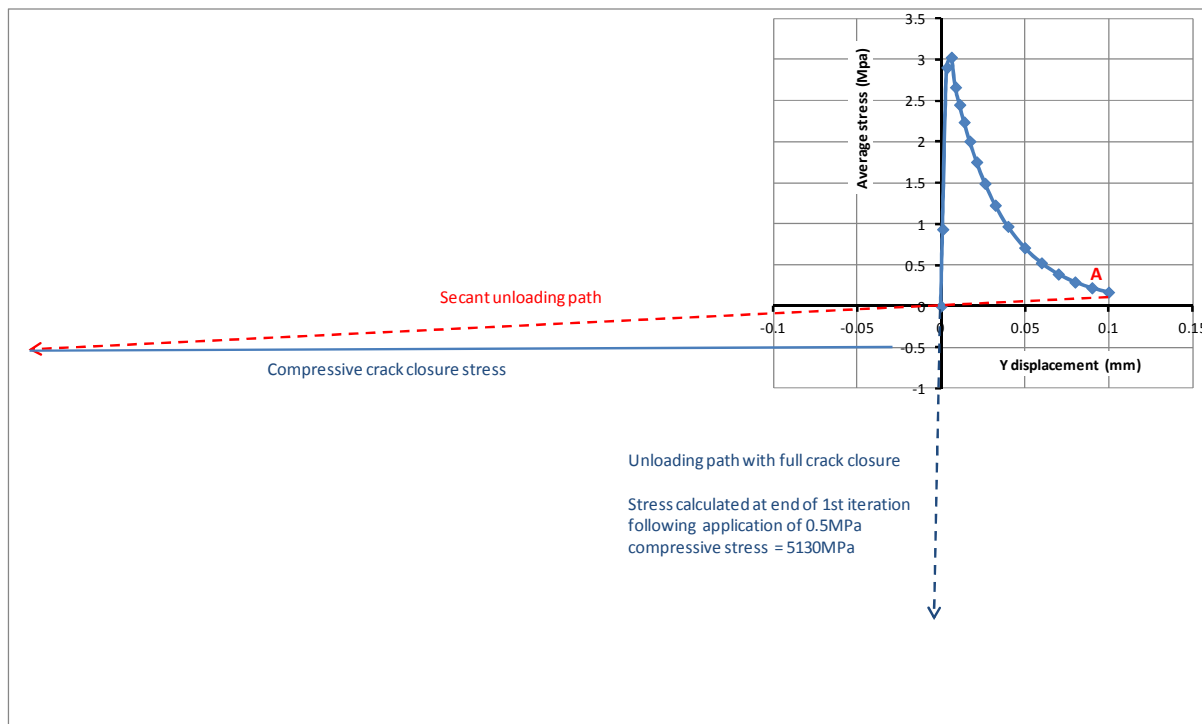Figure 1. Finite element mesh, dimensions and boundary conditions



Figure 2. Illustrative crack closure example

## 3. ROUGH CRACK MODEL WITH SMOOTH TRANSITION BETWEEN OPEN AND CLOSED CONTACT STATES

### 3.1 Basic crack-plane model

The model is described first for a 'crack-plane', which is defined as the mid surface of a narrow band of material that contains a macro-crack or a number of micro-cracks. It is assumed that the crack band is sufficiently narrow, relative to the principal structural dimensions, to be applicable to a zero thickness finite interface element or embedded discontinuity. When calibrating the model against test data, $h$ is taken to be equal to the width of a fracture process zone, which is typically 3 times the size of the coarse aggregate particles [7]. The local coordinate system of the crack plane is defined by the ortho-normal vectors $\mathbf{r}_1$ to $\mathbf{r}_3$ , as illustrated in Figure 3. The model relates the crack-plane traction vector ($\tilde{\boldsymbol{\tau}}$) to the relative displacement vector ($\tilde{\mathbf{u}}$), for which the elastic constitutive relationship is as follows:

$$\tilde{\boldsymbol{\tau}} = \tilde{\mathbf{k}}^e \tilde{\mathbf{u}}^e \tag{1}$$

in which the elastic constitutive matrix is defined as $\tilde{\mathbf{k}}^e = \begin{bmatrix} E/h & 0 & 0 \\ 0 & G/h & 0 \\ 0 & 0 & G/h \end{bmatrix}$, where $E$ and $G$ are Young's modulus

and the shear modulus of uncracked material respectively. Superscript $e$ denotes elastic and the overbar ~ denotes a crack-plane quantity. The three components of the vectors $\tilde{\boldsymbol{\tau}}$ and $\tilde{\mathbf{u}}$ coincide with the directions $\mathbf{r}_1$ to $\mathbf{r}_3$, such $\tilde{\tau}_1$ and $\tilde{u}_1$ are the components normal to the crack-plane and $\tilde{\tau}_2, \tilde{\tau}_3, \tilde{u}_2$ and $\tilde{u}_3$ are the in-plane components. We note that under linear elastic conditions $\tilde{\mathbf{u}}^e = \tilde{\mathbf{u}}$ .
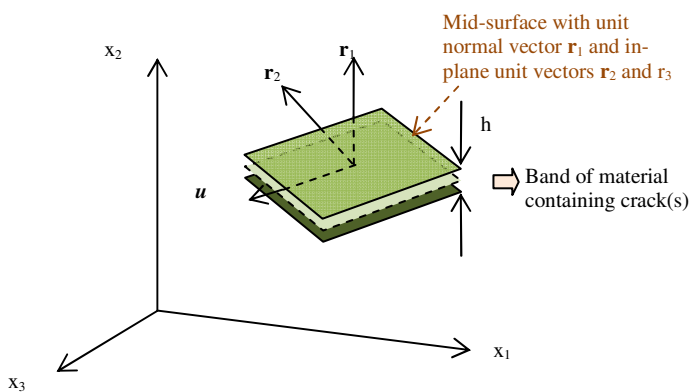


Figure 3. Crack plane and local coordinate systems.

The model assumes that, once a crack-plane has formed, the tractions have a damaged and an undamaged component as follows:

undamaged          damaged

$$\tilde{\boldsymbol{\tau}} \;=\; \big(1-\omega(Z)\big)\tilde{\boldsymbol{\tau}}_{\mathrm{u}} \;+\; \omega(Z)\tilde{\boldsymbol{\tau}}_{\mathrm{d}} \tag{2}$$

where $\omega \in [0,1]$ is the damage parameter, which is a function of the effective relative-displacement parameter $Z$.

The undamaged traction component $\tilde{\boldsymbol{\tau}}_{\mathrm{u}}$ is given by:

$$\tilde{\boldsymbol{\tau}}_{\mathrm{u}} = \tilde{\mathbf{k}}^{\mathrm{e}}\tilde{\mathbf{u}} \tag{3}$$

The evolution of $Z$ is governed by the following damage function, which is taken from reference [16]:

$$Z_{eq}(\tilde{u}) = \frac{\tilde{u}_1}{2}\left[1+\left(\frac{\mu}{\gamma}\right)^2\right] + \frac{1}{2\gamma^2}\sqrt{\left(\gamma^2-\mu^2\right)^2 \tilde{u}_1{}^2 + 4\gamma^2\left(\tilde{u}_2{}^2+\tilde{u}_3{}^2\right)} \tag{4a}$$

$$\varphi_d(\tilde{u},Z) = Z_{eq}(\tilde{u},Z) - Z \tag{4b}$$

with the standard loading/unloading conditions $\dot{Z}\geq 0; \quad \phi_d \leq 0; \quad \dot{Z}\cdot\phi_d = 0; \quad \dot{Z}\dot{\phi}_d = 0 \;\; \forall \;\; \phi_d = 0$

Also, $Z = \int_t \dot{Z}\,dt$ ; in which the superior dot denotes the time derivative and $t$ represents time.

The constants $\gamma$ and $\mu$ are the shear relative-displacement intercept and the asymptotic shear friction factor respectively of the damage surface in relative-displacement space. These are computed from the relative shear stress intercept ($r_\sigma = c/f_t$) and the asymptotic friction factor ($\mu_\sigma$); i.e. $\gamma = (E/G)\cdot r_\sigma$ and $\mu = (E/G)\cdot\mu_\sigma$; noting that $c$ is the shear stress intercept.  The damage surface, in terms of the local shear strains used in Section 5, together with further explanation of its derivation are given in Appendix D.

If applied to an interface, damage is initiated when $Z_{eq}$ first exceeds $Z_t$ , noting that $Z_t = h f_t/E$.

In a continuum model (Section 5), cracks are initiated using a principal stress criterion and the crack plane first forms in the major principal stress plane.

The damage evolution function is based on a standard exponential tensile softening function given by:

$$\omega(Z) = 1 - \frac{Z_t}{Z}e^{-c_1\left(\frac{Z-Z_t}{Z_m}\right)} \tag{5}$$

in which $Z_{\mathrm{m}}$ is the relative-displacement at the effective end of the uniaxial tensile softening curve (~0.2mm for normal concrete) and $c_1 = 5$. These parameters are determined from a direct fracture softening curve. $c_1$ is fixed at 5,

7

since this has been found to provide an acceptable match to a range of concrete data, and $Z_m$ may be determined directly from a softening curve or calculated from the specific fracture energy ($G_f$) using $Z_m \approx G_f \cdot c_1 / f_t$.

## 3.2 Rough contact component of the crack-plane model

### *Experimental evidence for an effective contact surface*

An examination of tests in which cracks are fully opened, held at a constant opening, and then loaded in shear show a distinct region in which the shear response stiffens rapidly [6,19,44], as illustrated in Figure 4. This response is attributed to the asperities of opposing surfaces regaining contact in shear and plotting the 'effective contact points' (circled in Figure 4) in relative-displacement space gives an 'effective contact surface'.

In the tests of Hazzenzadeh [21] and Jacobsen et al. [23] (Figures 5a and 5b), this shear stiffening behaviour is not as distinct as in the tests referred to above. This may be explained by the fact that the range of initial crack openings in these tests were significantly less than in the aforementioned work [6,19]. The cracks in these more recent tests were also (in general) not fully formed when shear was first applied and thus crack evolution would have been ongoing during the mixed mode loading phase. This means that the observed response resulted from a combination of rough contact behaviour and micro/macro crack evolution and in such tests it is much more difficult to isolate shear contact behaviour.  Notwithstanding this observation, these data suggest that there is limited loss of shear contact at small crack openings. A further relevant mechanism relates to small particles, displaced during normal cracking, that act as wedges bridging between opposing crack faces.
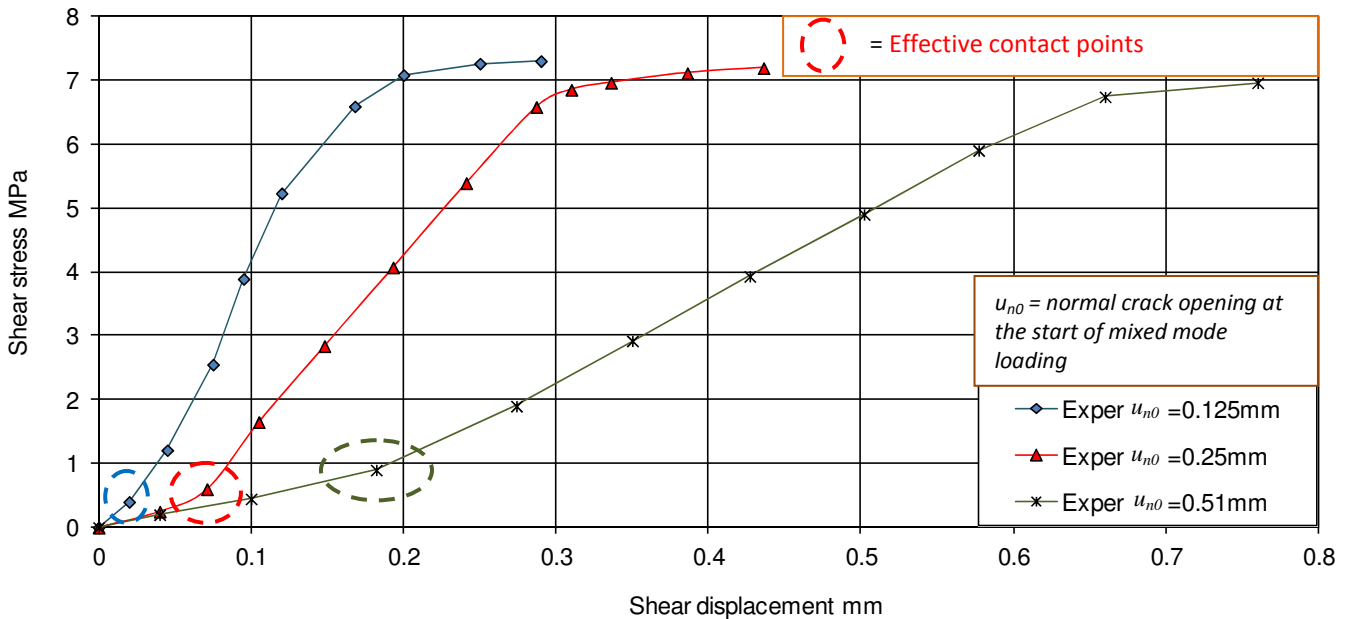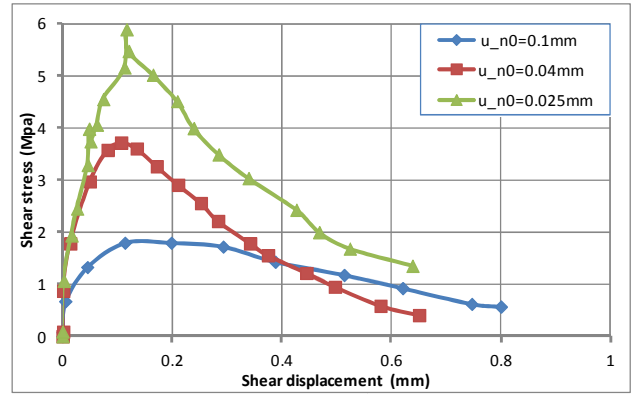


Figure 4. Shear contact transition zones from Paulay and Loeber's tests [6]
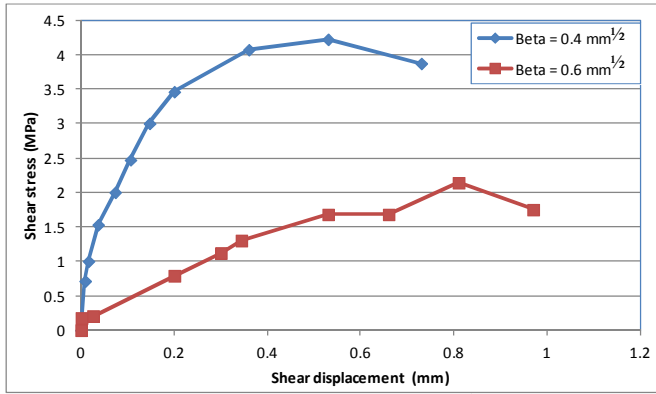
5a. Data from Hassanzadeh [21]                    5b Data from Jacobsen et al. [23]

Hassanzadeh's tests involved firstly applying tension to the point of first fracture and then applying displacements according to $u_n = \beta\sqrt{u_s}$. In Jacobsen et al.'s tests, a crack was first opened to a value of $u_{n0}$ and then combined mixed mode loading was applied such that $\Delta u_n / \Delta u_s = tan(\alpha)$. Data from the tests with $\alpha = 40^o$ are shown here. Note that $u_n$ (= $\tilde{u}_1$) and $u_s$ (= $\sqrt{\tilde{u}_2^2 + \tilde{u}_3^2}$) refer to normal and shear relative-displacements when plotting experimental data.

The following conclusions are drawn from our observations on the above shear-normal test data (Figures 4 and 5);

(i)      there is an effective contact surface in relative-displacement space with a positive slope in $u_n$ vs $u_s$ space;

(ii)     there is a region for small crack openings for which there is no measurable loss of shear contact.

These conclusions led to the derivation of the single smooth effective contact surface illustrated in Figure 6.



Figure 6. Effective contact surface and associated experimental data

9

## Effective contact function

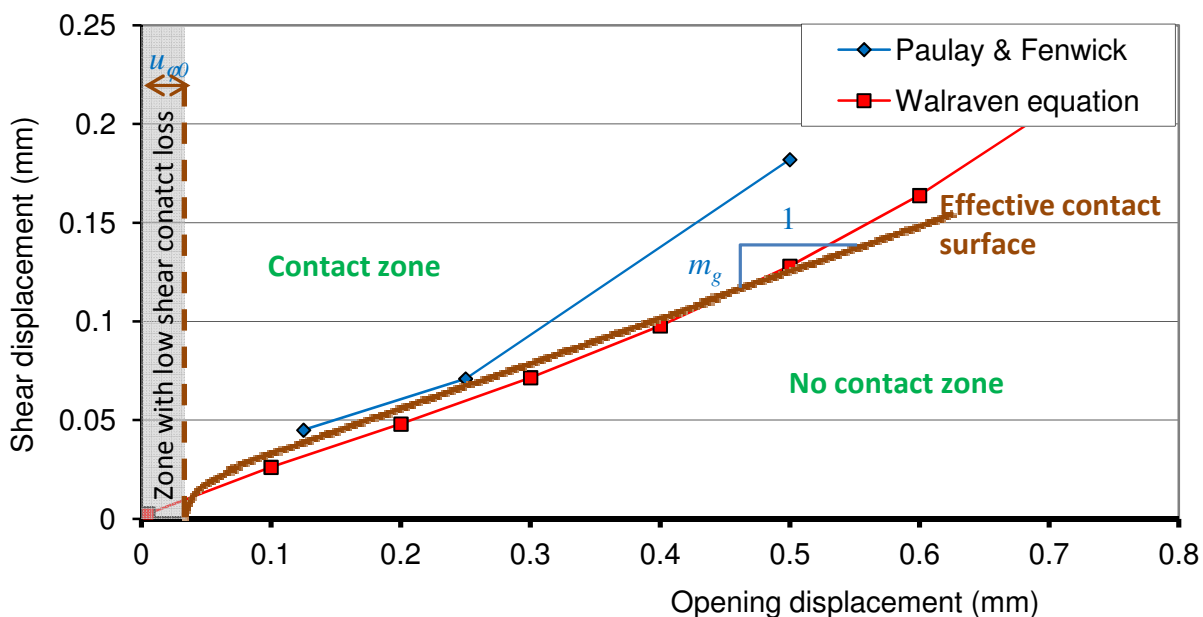For reasons that will be explained later in this section, it is advantageous to use a mathematical expression for the effective contact function ($\varphi(\tilde{\mathbf{u}})$) that has the properties (in relative-displacement space) of a signed distance function i.e.

$$\left|\frac{\partial \varphi}{\partial \tilde{\mathbf{u}}}\right| = 1 \tag{6}$$

$$\phi(\tilde{\mathbf{u}})\frac{\partial \varphi}{\partial \tilde{\mathbf{u}}} = \tilde{\mathbf{u}} - \tilde{\mathbf{u}}_c \tag{7}$$

in which $\tilde{\mathbf{u}}_c$ is the nearest point to $\tilde{\mathbf{u}}$ as illustrated in Figure 7.

The function chosen for $\varphi$ is selected to fit that shown in Figure 7 and comprises two parts, (i) formed by a spherical arc and (ii) that is a partial cone which is tangential to the arc. The interface between these two parts is governed by the function $\varphi_c$, which is defined as follows:

$$\varphi_c(\tilde{\mathbf{u}}, Z) = \frac{1}{\sqrt{1+m_g^2}}\left(\tilde{u}_1 - u_{\varphi c}(Z) + m_g\sqrt{\left(\tilde{u}_2^2 + \tilde{u}_3^2\right)}\right) \tag{8}$$

The contact function is then evaluated as follows:

$$\varphi = \frac{1}{\sqrt{1+m_g^2}}\left(m_g \cdot \left(\tilde{u}_1 - u_{\varphi i}(Z)\right) - \sqrt{\left(\tilde{u}_2^2 + \tilde{u}_3^2\right)}\right) \qquad \forall \quad \varphi_c(\tilde{\mathbf{u}}, Z) > 0$$

$$\varphi = \left(u_{\varphi c}(Z) - u_{\varphi 0}\right) - \sqrt{\left(\left(\tilde{u}_1 - u_{\varphi c}(Z)\right)^2 + \tilde{u}_2^2 + \tilde{u}_3^2\right)} \qquad \forall \quad \varphi_c(\tilde{\mathbf{u}}, Z) \leq 0 \tag{9}$$

in which $m_g$ defines the slope of the conical part of the contact function (See Figures 6 and 7).

In three dimensions, the effective contact surface takes the form of a round-nosed cone centred on the normal relative-displacement axis.

This two-part effective contact function is governed by the two other functions (illustrated in Figure 7) given in equations 10a,b:

$$u_{\varphi c}( Z )=n_g u_0 + u_{lm}( Z )+u_{\varphi 0}$$

$$u_{\varphi i}( \zeta_p )=\frac{m_g - \sqrt{1+m_g^2}}{m_g}\left( n_g u_0 + u_{lm}( Z )\right)$$

(10a,b)

in which the constant $n_g$ governs the radius of the reference surface for contact transition (see Figure 7) and the fixed value of $n_g$=0.025 was determined using the data for the contact surface given in Figure 6 and the contact transition data presented in Figure 8 below.

The function $u_{lm}(Z)$ is related to the transition function and will be given after the derivation of the crack-plane constitutive relationship and the new contact transition theory have been given.



Figure 7. The effective contact function

## *Cracked component tractions*

The effective contact function is now used to relate the crack-plane tractions to relative-displacements. In contact mechanics [64], the embedment (negative gap) between points on two opposing contacting surfaces is used to determine the contact force. The same idea is used here, except that the present effective contact surface is a representation of the centre of a zone in which multiple contacts and surface interactions are occurring.

Since the effective contact function has the properties of a signed distance function, the embedment relative-displacement ( $\Delta \tilde{\mathbf{u}} = \tilde{\mathbf{u}} - \tilde{\mathbf{u}}_c$ ) is given by:

$$\Delta \mathbf{u} = \varphi( \tilde{\mathbf{u}} )\frac{\partial \varphi}{\partial \tilde{\mathbf{u}}}$$

(11)

It then follows that the tractions on the crack surface (i.e. on the damaged portion of the surface) are given by:

$$\tilde{\boldsymbol{\tau}}_d = \mathbf{k}^e \varphi(\tilde{\mathbf{u}})\frac{\partial \varphi}{\partial \tilde{\mathbf{u}}}$$

(12)

11

## Contact reduction function

The amount of contact between opposing rough crack surfaces reduces as the crack opening increases. This is evident from Figures 4 and 5 which show that the wider a crack is open, the shallower the shear response curve. Mihai et al. [46], in their multi-asperity model, suggested that -for a set of asperities of height $h_{asp}$- the contact potential function ($H(\tilde{u}_1)$) should take the form $H(\tilde{u}_1) = (1 - \tilde{u}_1/h_{asp})^2$. However, an exponential function, which provides a close fit to this equation over the range of interest, is preferred here for numerical reasons. Also, since concrete contains coarse aggregate, fine aggregate and hardened cement paste (hcp), all with different size ranges, three sets of asperity heights are considered. Furthermore, if the observation that no significant contact is lost until $\tilde{u}_1$ reaches $u_{\varphi 0}$ is taken into account, the contact reduction function takes the form:

$$H(\tilde{u}_1) = \sum_{i=1}^{3} p_i e^{-(\tilde{u}_1 - u_{\varphi 0})/(c_i u_0)} \qquad \forall \quad \tilde{u}_1 \geq u_{\varphi 0}$$

$$H(\tilde{u}_1) = 1 \qquad \forall \quad \tilde{u}_1 < u_{\varphi 0}$$

(13a,b)

in which the parameters $p_1$, $p_2$ and $p_3$ nominally represent the proportions of shear transfer associated with the hcp, fine and coarse aggregate phases respectively; these being subject to the condition $\sum_{i=1}^{3} p_i = 1$. $c_1$, $c_2$ and $c_3$ are associated material parameters. Default values for these parameters (written as vectors for convenience) are $p = [0.6, 0.3, 0.1]^T$ and $c = [0.01, 0.05, 2.0]^T$. These parameters vary significantly with aggregate type, size and grading; and ideally they should be calibrated against data from shear tests on cracked concrete specimens with different openings. A further refinement to the model, not undertaken here, is to use multiple contact surfaces each with a different $m_g$ value. The method used to select the rough contact material parameters for the examples presented in Section 6 may be found in Section 5.4.

Including this contact reduction function in equation (12) gives the following revised function for the cracked surface traction vector:

$$\tilde{\boldsymbol{\tau}}_d = H(\tilde{\mathbf{u}}) \cdot \mathbf{k}^e \varphi(\tilde{\mathbf{u}}) \frac{\partial \varphi}{\partial \tilde{\mathbf{u}}}$$

(14)

## Smoothing the contact response

The discussion in Section 2 of this paper highlighted the problems associated with modelling abrupt contact and the potential benefits of smoothing this contact behaviour. Experimental evidence from crack opening–closing tests [27] shows that cracks open and close gradually over a $\tilde{u}_1$ region rather than instantaneously. Hence, the advantages of including smoothed (gradual) opening/closing behaviour in a crack plane model are twofold i.e. (i) it provides a more accurate response and (ii) it improves numerical robustness.

Crack opening–closing tests [27] also exhibit a hysteresis response but no attempt is made to simulate this aspect of behaviour here. The basic principles of the model would allow it to be extended for such hysteresis behaviour but these effects are considered second-order when modelling most reinforced concrete structures.

In order to provide a smooth transition between open and closed states, a transition function was derived by considering the change in the tangent stiffness from an open state ($k_u$) to a closed state ($k_u+k_c$) in an idealised 1D problem (See Appendix B for full derivation). This is achieved using a *tanh* function:

$$k_T(u) = k_u + k_c \left( \frac{1 - tanh\left( u/u_z \right)}{2} \right)$$

(15)

in which $u$ is a scalar displacement, $k_T(u)$ is the tangent 1D stiffness, and $k_u$ and $k_c$ represent the undamaged and contact components of stiffness respectively.

As shown in Appendix B, this leads to following transition function $\lambda(u)$, which, when applied to the crack plane, becomes a function of the value of the effective contact function ($\varphi$):

$$\lambda(\varphi) = \frac{1}{2} \left[ 1 - \frac{\varphi}{\varphi - u_{lm}} ln\left( \frac{cosh\left( \varphi/u_z \right)}{cosh(c_{lm})} \right) \right]$$

(16)

Experimental data [27] also suggest that the size of the transition region increases as cracking progresses. Selected data from the same test have been plotted in Figure 8, which shows the initial response to the first peak and three selected reloading responses. The approximate effective transition zones ($u_{ETZ}$) for the reloading curves have been extracted from this graph and plotted against the associated opening displacements (the maximum opening value associated with the unloading-reloading cycle) in Figure 9. The resulting graph was then used to calibrate the transition function. These data suggest that the following linear equation for the $u_{ETZ}$ is adequate:

$$u_{ETZ} = u_{ETZ_0} + Z/c_{ETZ}$$

(17)

in which $u_{ETZ_0} = 0.018$ and $c_{ETZ} = 6$ .

However, in equation (16), it is $u_z$ that governs the size of the transition zone and this does not equal $u_{ETZ}$. Numerical calibration gave the result that $u_z = 2/3 u_{ETZ}$, thus $u_z(Z)$ becomes:

$$u_z(Z) = u_{z0} + \frac{Z}{c_{zn}}$$

(18)

noting that $c_{zn} = 3c_{ETZ}/2$ (i.e. $c_{zn}=9$), $u_{z0} = u_{ETZ_0}$ and $u_z(Z)$ is limited to $u_{z0}+Z_m/c_{zn}$

$u_{lm}(Z)$ governs the effective start of the transition region from the 'open contact state' and is related to $u_z$:

$$u_{lm}(Z) = u_z(Z)/c_{lm} \tag{19}$$
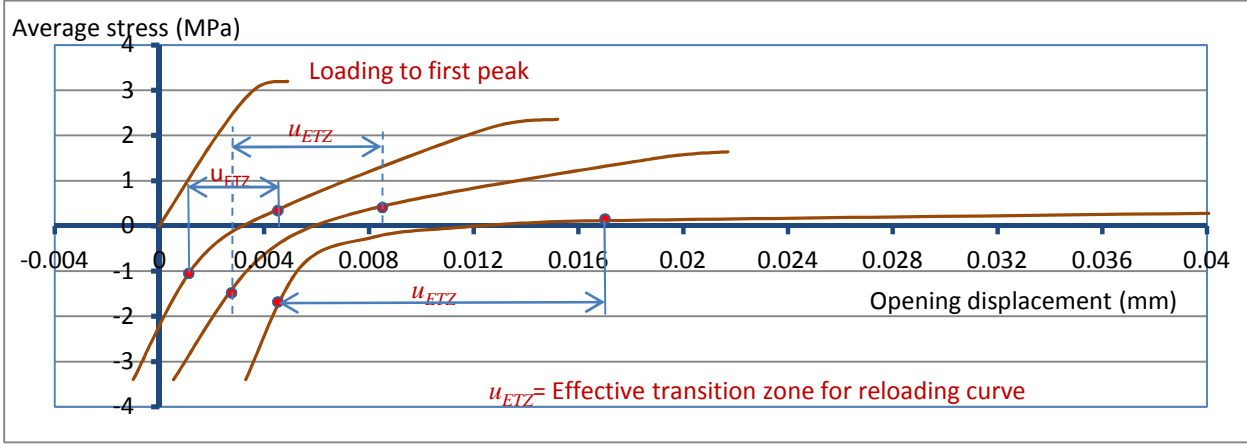
in which $c_{lm}=7$. (See Appendix B.)



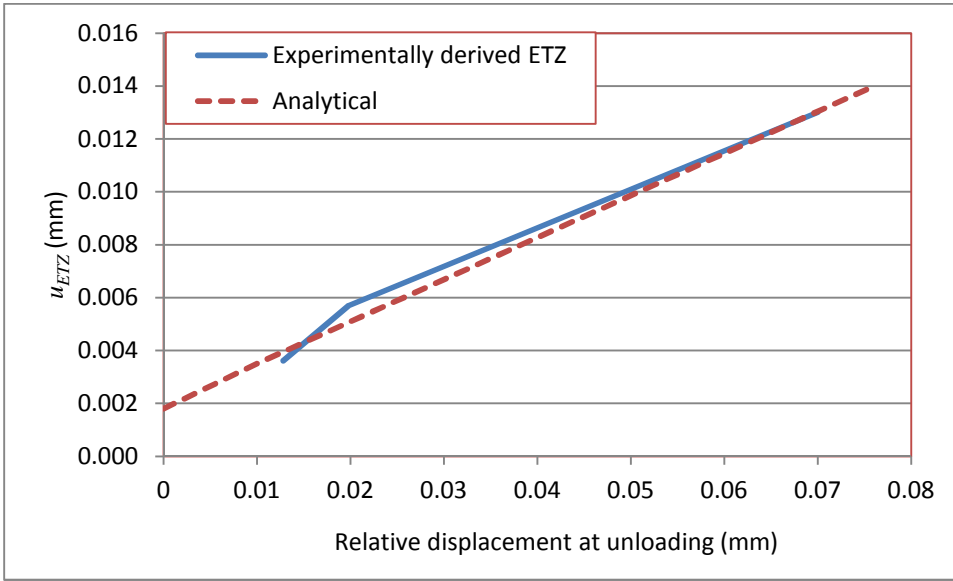Figure 8. Selected reloading curves from Reinhardt's tests [27].



Figure 9. Effective contact transition zone

Including the transition into the expression for the damage component tractions gives:

$$\tilde{\mathbf{\tau}}_d = \lambda(\varphi) \cdot H(\tilde{\mathbf{u}}) \cdot \mathbf{k}^e \left( \varphi(\tilde{\mathbf{u}}) - u_{lm} \right) \frac{\partial \varphi}{\partial \tilde{\mathbf{u}}} \tag{20}$$

14

*Final smoothed crack-plane constitutive relationship*

Using equations (20) and (3) in equation (2) gives the final form of the crack-plane constitutive relationship:

$$\tilde{\boldsymbol{\tau}} \;=\; \left(1-\omega(Z)\right)\cdot\tilde{\mathbf{k}}^{e}\tilde{\mathbf{u}} \;\;+\;\; \omega(Z)\cdot\lambda(\varphi)\cdot H(\tilde{\mathbf{u}})\cdot\tilde{\mathbf{k}}^{e}\left(\varphi(\tilde{\mathbf{u}})-u_{lm}\right)\frac{\partial\varphi}{\partial\tilde{\mathbf{u}}} \tag{21}$$

## 4. CRACK-PLANE MODEL RESPONSE

The behaviour of the crack-plane model is now illustrated for a set of idealised relative-displacement paths using the material data given in Table 1, with all other parameters taken as their default values. The computed response for these paths are shown in Figures 10 and 11, in which $\tau_n$ and $\tau_s$ represent the normal and shear crack-plane tractions respectively.

Path 1 comprises a series of loading–unloading cycles in direct tension (Figure 10).

Paths 2 and 3 (Figure 11) are cases in which a crack is opened in uniaxial tension (to $u_n$=0.06mm for path 2 and 0.122mm for path 3), then loaded in shear whilst $u_n$ remains constant.

Table 1. Material properties for crack-plane examples

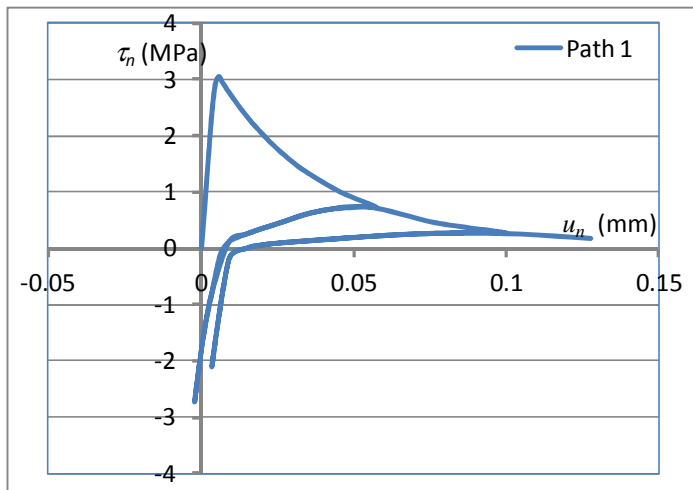| $h$ (mm) | $E$ kN/mm$^2$ | $\nu$ | $f_t$ N/mm$^2$ | $Z_m$ (mm) |
|---|---|---|---|---|
| 56 | 40 | 0.2 | 3 | 0.2 |



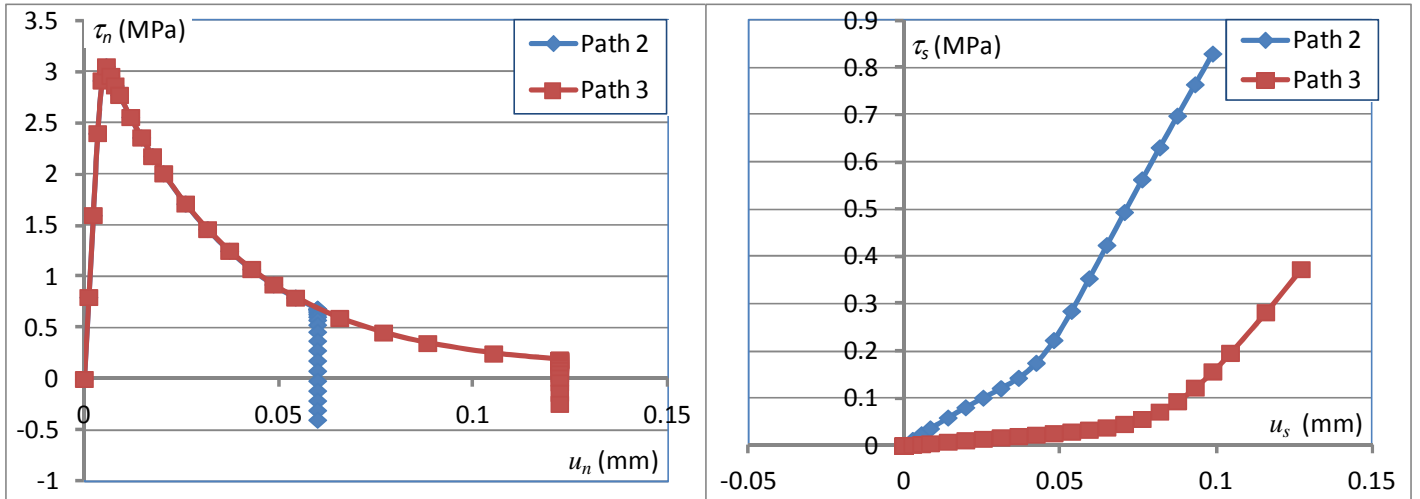Figure 10. Uniaxial opening and closing response.

Figure 11. Cracks opened in uniaxial tension and subsequently loaded in shear.

The smooth contact transition is evident in the direct tension unloading response in Path 1 and in the shear responses of Paths 2 and 3.

## 5. EMBEDDED CRACK-PLANES IN A 3D CONSTITUTIVE MODEL.

### 5.1 Embedded smeared cracks

When the crack-plane model is applied to continuum elements, cracks are effectively smeared over elements and are represented by directional damage. $h$ is no longer employed directly to define the local strains; instead, the crack-band approach of Bazant and Oh [3] is used. This involves scaling the governing fracture softening stress–strain curve, using the fracture energy parameter ($G_f$), such that the energy consumed in fully opening a mode 1 crack is the same irrespective of the element size. A key assumption in this method is that (numerically) strains localise into a band of elements, one element wide, early enough in the fracture process for the fracture energy consumed outside this band to be negligible. If this assumption is valid, the inelastic fracture strain vector (i.e. the reduced form of the strain tensor) can be related to the inelastic relative displacement vector ($\breve{\mathbf{u}}$) as follows:

$$\breve{\boldsymbol{\varepsilon}} = \frac{\breve{\mathbf{u}}}{\ell_{ch}} \tag{22}$$

in which $\ell_{ch}$ is the element characteristic length, $\breve{\mathbf{u}} = \tilde{\mathbf{u}} - \mathbf{u}^{e}$ and $\breve{\boldsymbol{\varepsilon}} = \begin{bmatrix} \breve{\varepsilon}_{11} & \breve{\varepsilon}_{12} & \breve{\varepsilon}_{13} \end{bmatrix}^{\mathrm{T}}$.

The characteristic length is equal to the length of the longest straight line that could be drawn within a finite element normal to the crack-plane. This gives a length in between that computed by 'Oliver's 1st and 2nd methods', which are described in References [52] and [65].

The element local strain vector ($\tilde{\boldsymbol{\varepsilon}}$) is then defined as the sum of the inelastic and elastic strain components:

$$\tilde{\boldsymbol{\varepsilon}} = \breve{\boldsymbol{\varepsilon}} + \boldsymbol{\varepsilon}^{e} \tag{23}$$

The smeared crack counterpart to equation (21) is :

$$\tilde{\boldsymbol{\sigma}} = \left(1 - \omega(\zeta)\right) \cdot \tilde{\mathbf{D}}^{e} \tilde{\boldsymbol{\varepsilon}} + \omega(\zeta) \cdot \lambda(\varphi) \cdot H_{c}(\tilde{\boldsymbol{\varepsilon}}) \cdot \tilde{\mathbf{D}}^{e} \cdot \left(\varphi(\tilde{\boldsymbol{\varepsilon}}) - \varepsilon_{lm}\right) \cdot \frac{\partial \varphi}{\partial \tilde{\boldsymbol{\varepsilon}}} \tag{24}$$

in which the effective strain parameter ($\zeta$) replaces $Z$, $\varepsilon_{lm} = u_{lm}/\ell_{ch}$, $H_{c}$ is the continuum form of the contact reduction function (see equation 25), the tractions are replaced by the local stresses ( $\tilde{\boldsymbol{\sigma}} = \begin{bmatrix} \tilde{\sigma}_{11} & \tilde{\sigma}_{12} & \tilde{\sigma}_{13} \end{bmatrix}^{\mathrm{T}}$ ) and

the local elastic constitutive matrix $\tilde{\mathbf{D}} = \begin{bmatrix} E & 0 & 0 \\ 0 & G & 0 \\ 0 & 0 & G \end{bmatrix}$.

The continuum form of the contact reduction function, denoted $H_{c}$ in equation (24), is different from the function $H$ used in equation (21). This is due to the fact that the inelastic slip across a crack-band in a mesh of continuum elements should be independent of element size in the same way that the inelastic crack opening should not depend on the mesh grading; the latter being addressed by the use of the crack-band approach. This is an issue that has previously been overlooked by the first author as well as by others who have used models in which the shear stiffness

17

of cracked elements is reduced with increasing crack opening. The function used for $H_c$, derived in Appendix C, is as follows:

$$H_c = \frac{H \cdot \ell_{ch}}{H \cdot \ell_{ch} + (1 - H) \cdot h} \tag{25}$$

Equation (25) introduces element 'shear-scaling' because the cracked shear stiffness depends on, or is scaled with, the element size. It is noted that the factor $H_c$ has no effect on the predicted response when mode 1 cracking is simulated.

The local stress–strain relationship, given in equation (24), can be written as:

$$\tilde{\boldsymbol{\sigma}} = \tilde{\mathbf{D}}^e \left( \mathbf{M}_s \tilde{\boldsymbol{\varepsilon}} + \tilde{\boldsymbol{\varepsilon}}_c \right) \tag{26}$$

where $\mathbf{M}_s = (1 - \omega) \cdot \mathbf{I}$ and $\tilde{\boldsymbol{\varepsilon}}_c = \omega \cdot \lambda \cdot H \cdot (\varphi - \varepsilon_{lm}) \cdot \dfrac{\partial \varphi}{\partial \tilde{\boldsymbol{\varepsilon}}}$ ; dependencies have been dropped for clarity.

The local fracture strain vector, in terms of the element local strain and stress vectors, is now given by:

$$\breve{\boldsymbol{\varepsilon}} = \tilde{\boldsymbol{\varepsilon}} - \tilde{\mathbf{C}}^e \tilde{\boldsymbol{\sigma}} \tag{27}$$

in which $\tilde{\mathbf{C}}^e = \tilde{\mathbf{D}}^{e-1}$

Using equation (26) in (27) to eliminate $\tilde{\boldsymbol{\varepsilon}}$ results in the following equation for the local fracture strain vector:

$$\breve{\boldsymbol{\varepsilon}} = \tilde{\mathbf{C}}_s \tilde{\boldsymbol{\sigma}} - \mathbf{M}_s^{-1} \tilde{\boldsymbol{\varepsilon}}_c \tag{28}$$

in which $\tilde{\mathbf{C}}_s = \left( \mathbf{M}_s^{-1} - \mathbf{I} \right) \tilde{\mathbf{C}}^e$

In order to derive an overall stress–strain relationship, the following transformation that relates the local stresses on a particular crack plane $j$ to the Cartesian stress tensor ($\boldsymbol{\sigma}$) is required:

$$\tilde{\boldsymbol{\sigma}}_j = \mathbf{N}(\mathbf{r}^j) \boldsymbol{\sigma} \tag{29}$$

where the transformation matrix $\mathbf{N}$ is defined in Appendix A.

The total stress and strain ($\boldsymbol{\varepsilon}$) tensors are represented in their reduced vector forms, i.e.

18

$$\boldsymbol{\sigma}=\begin{bmatrix}\sigma_{11} & \sigma_{22} & \sigma_{33} & \sigma_{12} & \sigma_{13} & \sigma_{23}\end{bmatrix}^{\mathrm{T}} \text{ and } \boldsymbol{\varepsilon}=\begin{bmatrix}\varepsilon_{11} & \varepsilon_{22} & \varepsilon_{33} & 2\varepsilon_{12} & 2\varepsilon_{13} & 2\varepsilon_{23}\end{bmatrix}^{\mathrm{T}}$$

in which the indices now relate to Cartesian directions.

The overall stress–strain relationship for a case with multiple cracks is then derived by subtracting the sum of the transformed fracture strain contributions (from all active crack planes) from the total strain tensor as follows:

$$\boldsymbol{\sigma} \;=\; \mathbf{D}_e\left(\boldsymbol{\varepsilon}-\sum_{j=1}^{n_p}\mathbf{N}_j^{\;T}\breve{\boldsymbol{\varepsilon}}_j\right) \tag{30}$$

in which $\mathbf{D}_e$ is the elastic tensor (in matrix form), $\breve{\boldsymbol{\varepsilon}}_j$ denotes the fracture strains for crack $j$, and $n_p$ is the number of crack planes at the current point (i.e. at a finite element integration point).

Using equations (28) and (29) in (30) and rearranging gives:

$$\boldsymbol{\sigma} \;=\; \mathbf{D}_e\left(\boldsymbol{\varepsilon}-\sum_{j=1}^{n_p}\mathbf{N}_j^{\;T}\left(\tilde{\mathbf{C}}_{s_j}\mathbf{N}_j\boldsymbol{\sigma}-\mathbf{M}_{s_j}^{\;-1}\tilde{\boldsymbol{\varepsilon}}_{c_j}\right)\right) \tag{31}$$

Taking the terms which pre-multiply $\boldsymbol{\sigma}$ to the left hand side of equation (31) gives:

$$\left(\mathbf{I}+\mathbf{D}_e\sum_{j=1}^{n_p}\mathbf{N}_j^{\;T}\tilde{\mathbf{C}}_{s_j}\mathbf{N}_j\right)\boldsymbol{\sigma} \;=\; \mathbf{D}_e\left(\boldsymbol{\varepsilon}+\sum_{j=1}^{n_p}\mathbf{N}_j^{\;T}\mathbf{M}_{s_j}^{\;-1}\tilde{\boldsymbol{\varepsilon}}_{c_j}\right) \tag{32}$$

Equation (32) may then be rearranged to give the following overall stress–strain relationship:

$$\boldsymbol{\sigma} \;=\; \left(\mathbf{I}+\mathbf{D}_e\sum_{j=1}^{n_p}\mathbf{N}_j^{\;T}\tilde{\mathbf{C}}_{s_j}\mathbf{N}_j\right)^{-1}\mathbf{D}_e\left(\boldsymbol{\varepsilon}+\sum_{j=1}^{n_p}\mathbf{N}_j^{\;T}\mathbf{M}_{s_j}^{\;-1}\tilde{\boldsymbol{\varepsilon}}_{c_j}\right) \tag{33}$$

## 5.2 Consistent tangent matrix

To derive the consistent tangent matrix for the model, the following incremental form of the crack-plane relationship (26) is used:

$$\delta\tilde{\boldsymbol{\sigma}}=\tilde{\mathbf{D}}^e\left(\mathbf{M}_s+\frac{\partial\mathbf{M}_s}{\partial\tilde{\boldsymbol{\varepsilon}}}\circ\tilde{\boldsymbol{\varepsilon}}+\frac{\partial\tilde{\boldsymbol{\varepsilon}}_c}{\partial\tilde{\boldsymbol{\varepsilon}}}\right)\delta\tilde{\boldsymbol{\varepsilon}}=\tilde{\mathbf{D}}^e\mathbf{M}_s{}'\delta\tilde{\boldsymbol{\varepsilon}} \tag{34}$$

in which $\circ$ denotes a third-order-matrix vector contraction.

The incremental fracture strains are then given by equation (35):

19

$$\delta\tilde{\boldsymbol{\varepsilon}} = \delta\tilde{\boldsymbol{\varepsilon}} - \tilde{\mathbf{D}}^{e-1}\delta\tilde{\boldsymbol{\sigma}} = \left(\mathbf{M}_s^{'-1} - \mathbf{I}\right)\tilde{\mathbf{C}}^e\delta\tilde{\boldsymbol{\sigma}} = \tilde{\mathbf{C}}'\delta\tilde{\boldsymbol{\sigma}} \tag{35}$$

The incremental form of the constitutive relationship (30) is:

$$\delta\boldsymbol{\sigma} = \mathbf{D}_e\left(\delta\boldsymbol{\varepsilon} - \sum_{j=1}^{n_p}\left(\mathbf{N}_j{}^T\delta\tilde{\boldsymbol{\varepsilon}}_j + \delta\mathbf{N}_j{}^T\tilde{\boldsymbol{\varepsilon}}_j\right)\right) \tag{36}$$

In the present approach $\delta\mathbf{N}_j$ is always set to **0**. This is justified because, in the iteration process, crack directions are fixed within the step in which they are formed after a fixed number of iterations, provided that a certain convergence tolerance (typically 100 times the overall convergence tolerance) has been reached.

Using (35) in (36) and rearranging gives the following consistent incremental stress–strain relationship;

$$\delta\boldsymbol{\sigma} = \left(\mathbf{I} + \mathbf{D}_e\left(\sum_{j=1}^{n_p}\mathbf{N}_j{}^T\tilde{\mathbf{C}}'_j\mathbf{N}_j\right)\right)^{-1}\mathbf{D}_e\delta\boldsymbol{\varepsilon} \tag{37}$$

## 5.3 Stress recovery procedure

A principal stress cracking criterion is used for crack initiation and the formation of cracks is systematically checked one at a time during the overall stress recovery procedure.

The introduction of the smooth contact formulation into the model simplifies the stress computation algorithm because, unlike that described in reference [16], there is no need to check the contact conditions. This is because the contact transition function ($\lambda(\varphi)$) is continuous and tends to zero in the no-contact region, as φ increases, but tends to unity in the closed region as φ becomes more negative.

To compute the stresses from equation (30), the fracture strains are required and these in turn depend upon the crack-plane strains $\tilde{\boldsymbol{\varepsilon}}_i$ according to the following relationship which may be deduced from equations (26) and (27):

$$\breve{\boldsymbol{\varepsilon}}_i = \left(\mathbf{I} - \mathbf{M}_{s_i}\right)\tilde{\boldsymbol{\varepsilon}}_i - \tilde{\boldsymbol{\varepsilon}}_{c_i} \tag{38}$$

The crack-plane strains are computed such that the crack-plane stress–strain relationship and the overall stress–strain relationship are both satisfied. This is accomplished by solving the following nonlinear coupled set of equations for all the cracks that exist at a particular integration point (*i=1 to n_p*):

$$\mathbf{N}_i\boldsymbol{\sigma} - \tilde{\boldsymbol{\sigma}}_i = \mathbf{0} \tag{39}$$

Equation (39) is expanded using equations (26), (28) and (30) to give:

$$\mathbf{N}_i \mathbf{D}_e \left( \boldsymbol{\varepsilon} - \sum_{j=1}^{n_p} \mathbf{N}_j^{\ T} \left( \mathbf{I} - \mathbf{M}_{s_j} \right) \tilde{\boldsymbol{\varepsilon}}_j - \tilde{\boldsymbol{\varepsilon}}_{c_j} \right) - \tilde{\mathbf{D}}^e \left( \mathbf{M}_{s_i} \tilde{\boldsymbol{\varepsilon}}_i + \tilde{\boldsymbol{\varepsilon}}_{c_i} \right) = \mathbf{0} \tag{40}$$

This set of nonlinear equations is solved using a Newton–Raphson procedure to obtain the crack-plane strains ($\tilde{\boldsymbol{\varepsilon}}_i$).

This involves expressing the error in equation (40) by the following local stress error vector ($\boldsymbol{\psi}_i$):

$$\boldsymbol{\psi}_i = \mathbf{N}_i \mathbf{D}_e \left( \boldsymbol{\varepsilon} - \sum_{j=1}^{n_p} \mathbf{N}_j^{\ T} \left( \mathbf{I} - \mathbf{M}_{s_j} \right) \tilde{\boldsymbol{\varepsilon}}_j - \tilde{\boldsymbol{\varepsilon}}_{c_j} \right) - \tilde{\mathbf{D}}^e \left( \mathbf{M}_{s_i} \tilde{\boldsymbol{\varepsilon}}_i + \tilde{\boldsymbol{\varepsilon}}_{c_i} \right) \tag{41}$$

Writing (41) as a first order Taylor's expansion, equating this to zero and rearranging the resulting equation, gives the iterative update in the stacked local strain vector as follows:

$$\delta \tilde{\mathbf{E}} = \mathbf{B}_E^{-1} \boldsymbol{\Psi} \left( \tilde{\mathbf{E}} \right) \tag{42}$$

in which $\tilde{\mathbf{E}} = \begin{bmatrix} \tilde{\boldsymbol{\varepsilon}}_1 \\ \tilde{\boldsymbol{\varepsilon}}_2 \\ : \end{bmatrix}$ and $\boldsymbol{\Psi} = \begin{bmatrix} \boldsymbol{\psi}_1 \\ \boldsymbol{\psi}_2 \\ : \end{bmatrix}$

The sub-matrix components of the matrix of derivatives are given by:

$$\mathbf{B}_{Ei,j} = \mathbf{N}_i \mathbf{D}_e \mathbf{N}_j^{\ T} \left( \mathbf{I} - \mathbf{M}'_{s_j} \right) + \tilde{\mathbf{D}}_{t_i} \partial_{i,j} \tag{43}$$

in which $\partial_{i,j}$ is the Kronecker delta, $\tilde{\mathbf{D}}_{t_i} = \tilde{\mathbf{D}}^e \mathbf{M}'_{s_i}$ and $i$ & $j$ are crack numbers.

The steps followed to solve these equation are outlined in Algorithm Box 1.

Box 1. Algorithm for updating crack plane variables and computing the Cartesian stress vector.

| | |
|---|---|
| $\tilde{\boldsymbol{\varepsilon}}_j = \tilde{\boldsymbol{\varepsilon}}_j{}^{prev}$ ; $\zeta_j = \zeta_j{}^{prev}$ | Set crack-plane parameters to previous values or initial values for a new crack. |
| **for** *iter*=1 to *Maxit* | Enter iteration loop |
| **for** *i*=1 to $n_p$ | Loop over crack-planes |
| $\omega(\zeta_i)$; $\varepsilon_{lm}(\zeta_i)$; $\varphi(\tilde{\boldsymbol{\varepsilon}}_i)$; $\lambda(\varphi_i)$ ; $H_c(\tilde{\boldsymbol{\varepsilon}}_i)$ ; $\boldsymbol{\varepsilon}_c(\tilde{\boldsymbol{\varepsilon}}_i)$; $\mathbf{M}_{s_i}(\zeta_i)$ | Compute crack-plane functions and matrices from equations (5), (19), (9), (16), (13&25), and (26) [Note 1]. |
| **for** *i*=1 to $n_p$ ; $\boldsymbol{\psi}_i(\tilde{\mathbf{E}})$ ; **end for** *i* | Compute the local stress error vector from equation (41) |
| **If** $\left\|\boldsymbol{\Psi}(\tilde{\mathbf{E}})\right\| < tol_\psi$ **Exit** iter loop | Check for convergence and exit loop if converged. [Note 2] |
| **Else** | |
| **if** *iter*=*Maxit*, **Exit** and reduce increment step size | Exit procedure and reduce global step size if iteration limit reached. [Notes 3] |
| **Else** continue with update | |
| **for** *i=1* to $n_p$ ; **for** *j=1* to $n_p$ ; compute $\mathbf{B}_{E_{i,j}}$ ; **endfor** *i* ; **endfor** *j* | Evaluate differential sub-matrices |
| $\delta\tilde{\mathbf{E}} = \mathbf{B}_E{}^{-1}\boldsymbol{\Psi}(\tilde{\mathbf{E}})$ | Solve equations for stacked vector of crack-plane strains |
| **for** *i=1* to $n_p$ | |
| $\tilde{\boldsymbol{\varepsilon}}_i = \tilde{\boldsymbol{\varepsilon}}_i + \delta\tilde{\boldsymbol{\varepsilon}}_i$ | Update crack-plane strains |
| **if** $\zeta_{eq}(\tilde{\boldsymbol{\varepsilon}}_i) > \zeta$ ; $\zeta := \zeta_{eq}(\tilde{\boldsymbol{\varepsilon}}_i)$ | Update effective crack plane strain parameter |
| Compute $\breve{\boldsymbol{\varepsilon}}_i$ | Compute the fracture strains from equation (38) |
| **endfor** *i* | |
| Compute $\boldsymbol{\sigma}$ | Compute Cartesian stresses from equation (30) |
| **end if** | |
| **endfor** *iter* | |

Notes:

1. When the original equations referenced are expressed in terms of relative-displacements, it is assumed that the equivalent local strain components are substituted here for the comparable relative-displacement components. (See Section 5.1).

2. *maxit*= 15 and $tol_\psi = f_t \times 10^{-6}$

3. This iteration limit was not exceeded in any of the examples presented in this paper.

22

## 5.4 Material parameters

The embedded smoothed crack-plane model requires a number of standard parameters as well as a few non-standard material parameters. Table 2 provides a summary of these parameters along with suggested values and some comments on how these parameters may be determined.

Table 2. Material parameter details

| Symbol | Description | Typical value for concrete | Comments |
|---|---|---|---|
| $E$ | Young's modulus. | 35000 N/mm$^2$ | Standard material constant |
| $v$ | Poisson's ratio | 0.2 | Standard material constant |
| $f_c$ | Uniaxial compressive strength | 40 N/mm$^2$ | Standard material constant |
| $f_t$ | Uniaxial tensile strength | 3 N/mm$^2$ | Standard material constant |
| $G_f$ | Fracture energy per unit area | 0.1 N/mm | Standard material constant |
| $m_g$ | Constant in interlock state function | 0.425 | This defines the slope of the contact surface cone, as shown in Figure 6. This may be determined by using tests in which shear loading is applied to specimens with fully formed cracks at different opening displacements. (See Section 3.2) |
| $h$ | Physical fracture process zone width | 60mm | This is taken to be 3x coarse aggregate size. |
| $r_{\boldsymbol{\sigma}}$ | Shear intercept to tensile strength ratio for local damage surface | 1.25 | Constants $r_{\boldsymbol{\sigma}}$ and $\mu_{\boldsymbol{\sigma}}$ govern the shape of the damage function, as shown in Appendix D. To determine the values directly, experimental data from shear tests on mortar – rock interfaces are required, appropriate to the type of concrete being analysed. This is rarely done and the values quoted here have been previously obtained for the model described in reference [16] by inversely identifying parameters that accurately represent crack growth under mixed mode conditions. |
| $\mu_{\boldsymbol{\sigma}}$ | Limiting friction ratio on which damage surface is based | 0.8 | |
| $[c_1,c_2,c_3]$ | Shear contact reduction parameters | [0.01, 0.05, 2.0] | $c_1,c_2,c_3$ are multipliers (on $\varepsilon_0$, or $u_0$) that control how shear contact potential reduces with increasing crack opening for hcp, fine aggregate and coarse aggregate phases respectively. (See equation 13). |
| $[p_1,p_2,p_3]$ | Shear contact proportion parameters | [0.6, 0.3, 0.1] | $p_1$, $p_2$ & $p_3$ nominally represent the proportions of shear transfer associated with the hcp, fine and coarse aggregate phases respectively. (See equation 13) <br><br> The values of $c_i$ and $p_i$ can calibrated using tests in which cracks are opened under normal loading and then loaded in shear. <br><br> Ideally data from separate tests on samples made of just hcp, mortar and concrete are required for a full calibration of the c and p constants. However, as yet, no such comprehensive set of data exists. Thus, the values have been calibrated using inverse parameter identification methods from existing shear-normal crack tests (See Section 3.2). An attempt to determine such parameters directly for a detailed micro-mechanical interface model is described in reference [46]. |

# 6. EXAMPLES

## 6.1 Introduction

All of the examples to be presented in this section have employed the continuum version of the model implemented in the finite element program LUSAS [66] via LUSAS's material model interface.

The first example presents an idealised cracking problem to demonstrate that the new continuum form of the contact reduction function (See equation 25 and Appendix C) gives mesh independent crack shear sliding behaviour.

A range of unreinforced concrete fracture tests are then considered in Examples 2 to 4. Example 2 shows an analysis of one of Reinhardt's cyclic notched fracture specimens; Example 3 considers the recent tests undertaken by Jacobsen et al. [23] and the fourth example presents a 3D analysis of one of Walravren and Reinhardt's [19] specimens in which shear loading was applied to a specimen with a preformed crack.

The material parameters used for all examples are given in Table 3. A Newton-based incremental iterative scheme was used to solve the nonlinear finite element equations with a tolerance of 0.01% for both the L2 iterative displacement and out of balance force norms. All 2D meshes comprised bilinear quadrilateral elements and the 3D mesh used trilinear hexahedral elements. The number of increments used in each example is evident from the response curve graphs, with markers showing the result at each increment solved.

Table 3. Concrete material properties

| Example | $E$ | $\nu$ | $f_c^*$ | $f_t$ | $G_f$ | $m_g$ | $h$ | $r_\sigma$ | $\mu_\sigma$ | $c_1$ $c_2$ $c_3$ | $p_1$ $p_2$ $p_3$ |
|---|---|---|---|---|---|---|---|---|---|---|---|
| | GPa | | MPa | MPa | N/mm | | mm | | | | |
| 1 | 40 | 0.2 | 40 | 3.0 | 0.12 | 0.3 | 60 | 1.25 | 0.8 | 0.01 0.05 2.0 | 0.6 0.3 0.1 |
| 2 | 35 | 0.2 | 50 | 3.2 | 0.12 | 0.3 | 60 | 1.25 | 0.8 | 0.01 0.05 2.0 | 0.6 0.3 0.1 |
| 3 | 41 | 0.2 | 35 | 3.0 | 0.08 | 0.18 | 20 | 1.25 | 0.8 | 0.01 0.06 0.3 | 0.2 0.4 0.4 |
| 4 | 25 | 0.2 | 23 | 2.5 | 0.10 | 0.28 | 60 | 1.25 | 0.8 | 0.01 0.05 2.0 | 0.6 0.3 0.1 |

*Compressive strength is given for reference only, since no crushing was simulated in any of the examples.

## 6.2 Examples

### Example 1. Idealised sandwich panel.

The first example is an idealised problem designed to illustrate the effects of using element shear scaling in the contact reduction function. This idealised specimen comprises a band of cracking material sandwiched between two bands of linear elastic material. The upper and lower boundaries are assumed to be fixed to rigid platens via which the specimen is loaded, as shown in Figure 12. The analysis sequence involves applying a normal displacement to the upper platen (to form cracks in the central band of material) and then, without changing the normal displacement, applying a shear displacement. The three meshes used for the analysis are shown in Figure 13, in which $h_e$=100, 50 and 25mm respectively. Analyses are performed 'with shear scaling' (i.e. using $H_c$ from equation (25)) and without shear scaling (i.e. using $H$ from equation (13)).

The computed normal response, shown in Figure 14, does not change with the introduction of shear scaling, since no contact occurs in this phase of loading. Figures 15a & 15b show that mesh-dependent shear behaviour is present when contact shear-scaling is not included; however, it is eliminated when shear-scaling is included.
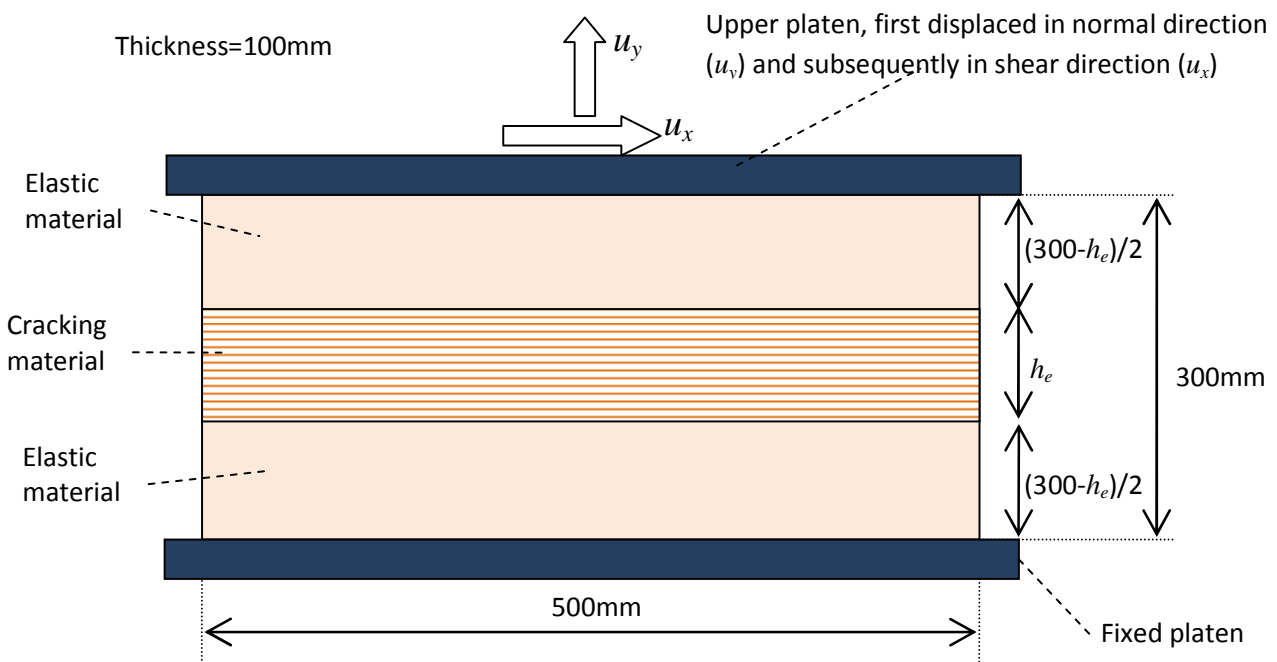


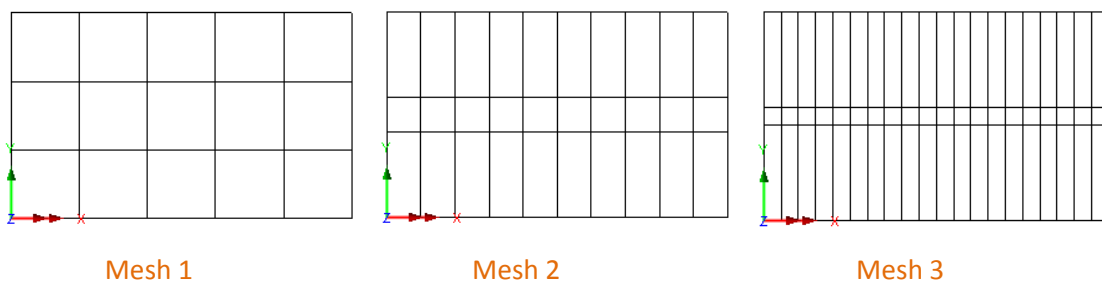Figure 12. Idealised arrangement considered in Example 1



Mesh 1          Mesh 2          Mesh 3
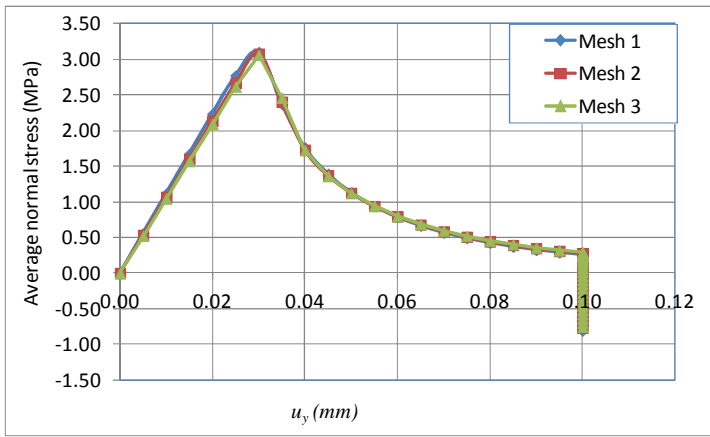
Fig 13 Finite element meshes

25

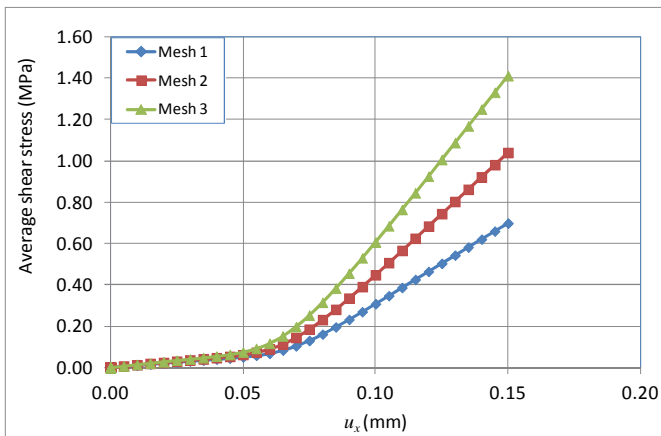Figure 14. Normal response (same with and without 'shear scaling')



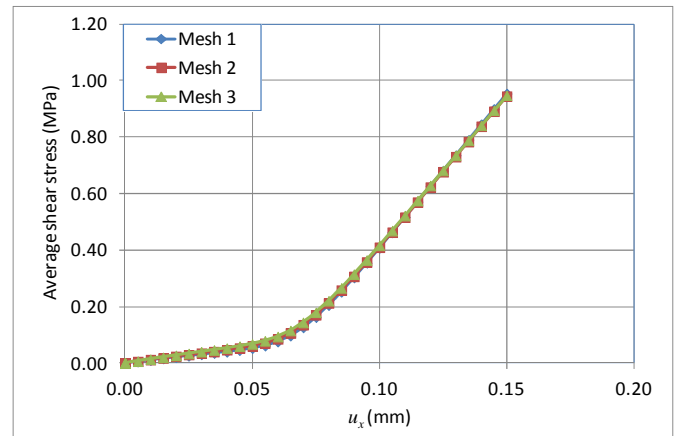Figure 15a. Shear response without 'shear contact scaling'

Figure 15b. Shear response with 'shear contact scaling'

*Example 2. Reinhardt's cyclic tension test.*

In this example a comparison is made with data from Reinhardt 's [27] LCLS (Large Compressive Lower Stress) test series on notched fracture specimens subjected to cyclic loading. The specimen and the mesh used for the analysis are shown in Figure 16.
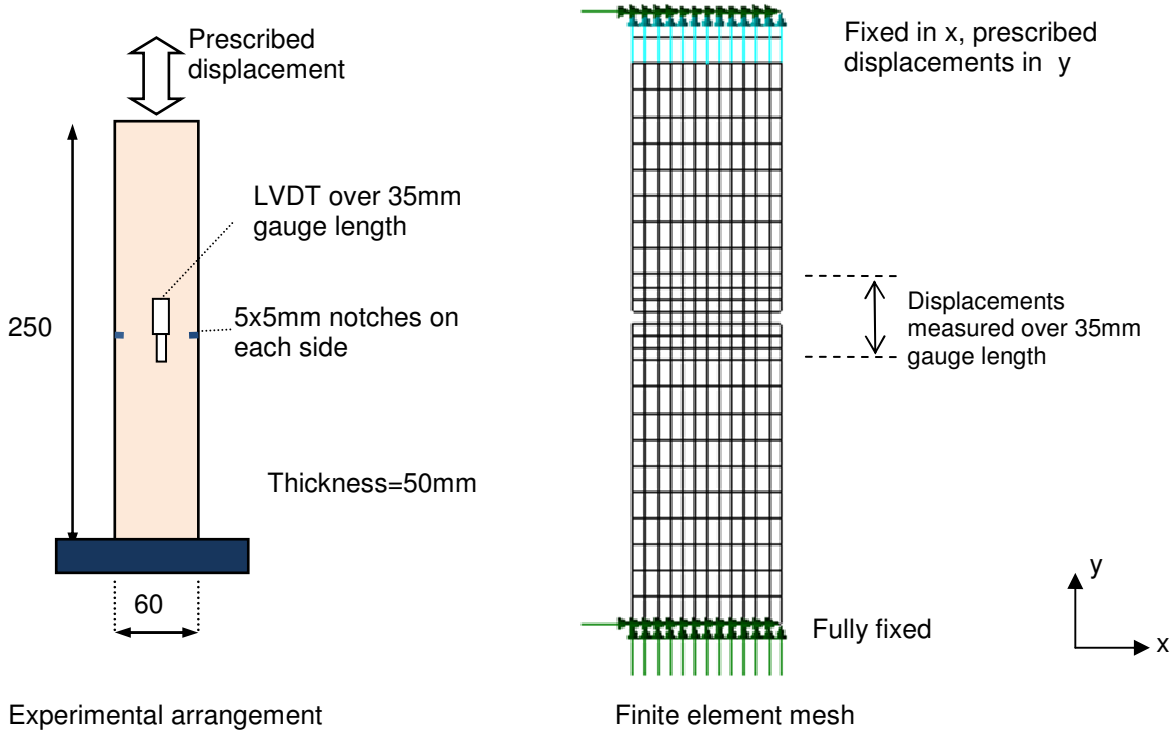
Figure 16. Experimental arrangement and finite element mesh for Example 2.

Figure 17 shows a comparison between the 'average stress' which, as in the original paper [27], is taken as the total reaction in the *y* direction divided by the area between the notches (50x50mm). A deformed mesh plot showing contours of the maximum crack opening displacement is given in Figure 18. As mentioned in Section 2, the present model does not simulate the hysteresis behaviour seen in such experiments but aims to match the reloading response and to use this for both unloading and reloading. Given this restriction, the model is considered to provide a good match to the experimental data. A final note on these results is that any apparent hysteresis in the numerical results is simply due to the fact that different relative-displacement values are used in the unloading and reloading parts of each cycle.
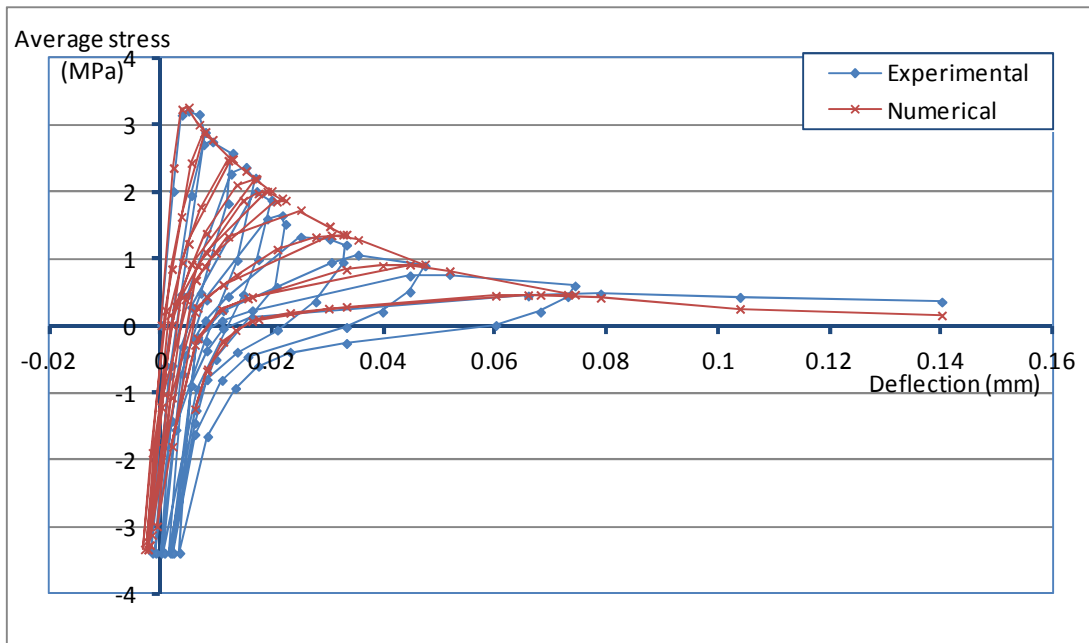
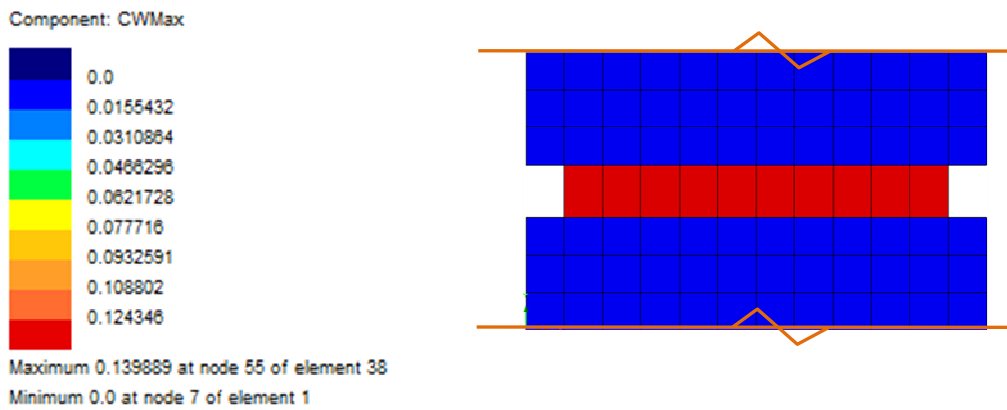Figure 17. Cyclic tension experimental and numerical responses



Figure 18. Deformed mesh plot at the final step showing crack opening displacements

*Example 3. Mixed mode tests of Jacobsen et al.*

Example 3 is based on a series of tests undertaken by Jacobsen et al. [23] on notched plain concrete specimens. As illustrated in Figure 19, these were first subjected to a normal opening displacement $u_{n0}$ and subsequently subjected to mixed mode loading with the ratio between normal and shear incremental displacements being $\tan(\alpha)$. The series of tests with $\alpha=40^{o}$ is considered here. The relative shear and normal displacements across the crack were measured by both a series of clip gauges and by a DIC (Digital Image Correlation) system [23]. The finite element mesh used for the analyses is illustrated in Figure 20.

Loaded to prescribed crack normal opening $un0$
Then loaded in mixed mode with $\Delta u_n / \Delta u_s = \tan(\alpha)$
Cases $un0$=0.025mm       $\alpha$=**40** → $60°$
       0.040mm
       0.10 mm

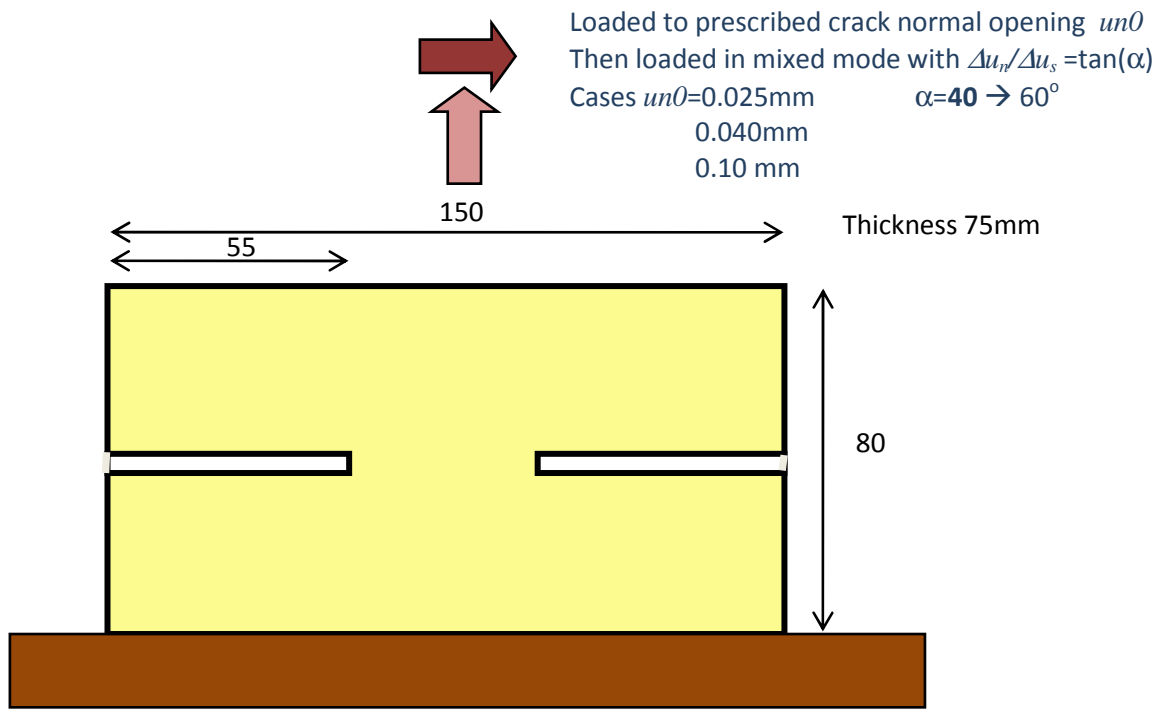Thickness 75mm

150
55
80

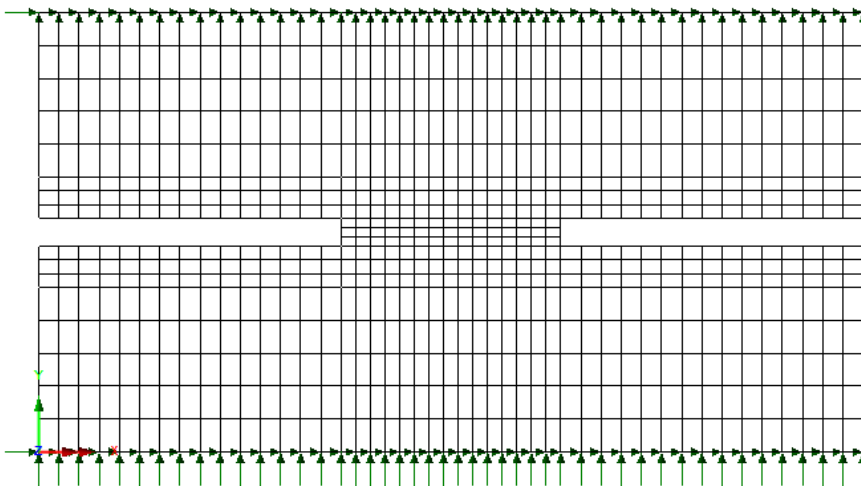Figure 19. Experimental arrangement



Figure 20. Finite element mesh

The experimental and numerical results in terms of average shear and normal stresses across the central crack area (40x75mm on plan) versus their associated relative displacements are shown in Figure 21. These plots show that the model captures the shear contact behaviour exhibited in these tests with good accuracy, especially when the natural variability of experimental data for this type of test is considered. In all cases the strains localised to the central band of elements, as illustrated in the deformed mesh plot shown in Figure 22, which shows the crack opening

displacement at approximately $u_n$=0.4mm for the analysis case with $u_{n0}$=0.025mm. The numerical crack plots are consistent with the experiments, in which a dominant cracks formed between the notches.
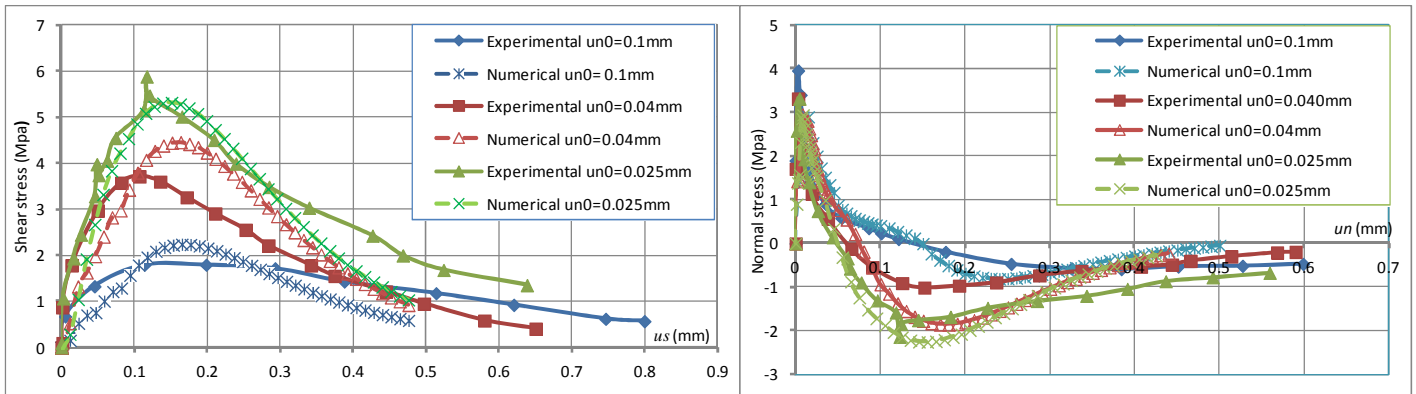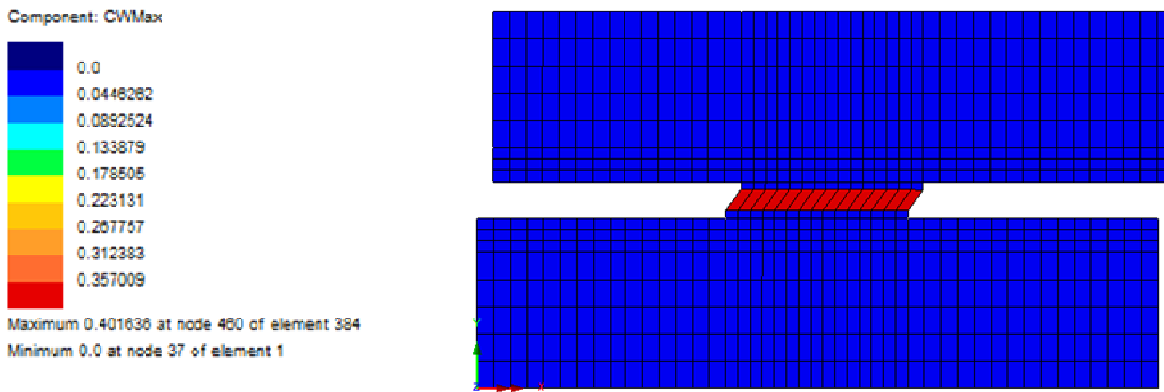


Figure 21. Shear and normal responses



Figure 22. Deformed mesh showing the maximum crack opening for the $u_{n0}$=0.025mm analysis case.

*Example 4. Shear tests on a cracked concrete specimen by Walraven and Reinhardt*

The final example presents a simulation of one of the cracked concrete specimens tested by Walraven and Reinhardt [19]. The specimens used in these tests had a shear plane of 300x120 mm$^2$ and were tested in a stiff testing frame with external restraint bars, which controlled the normal crack opening. Initial cracks were formed by using a splitting technique. The test code a/b/c gives 'a' the concrete mix number, 'b' the nominal opening and 'c' the normal stress. The testing arrangement and the (somewhat idealised) 3D mesh used for the analysis are shown in Figures 23a and b respectively.
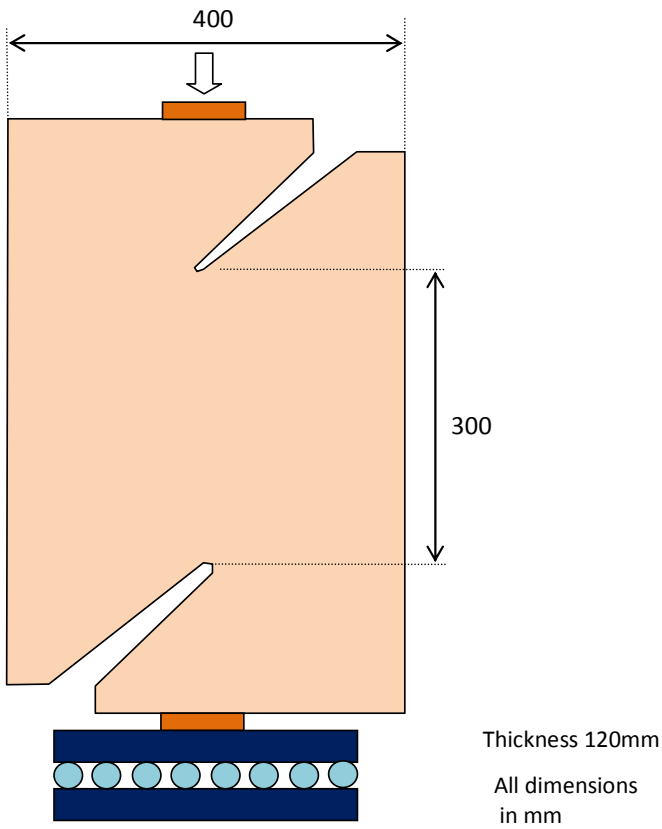
30

Figure 23a Testing arrangement.
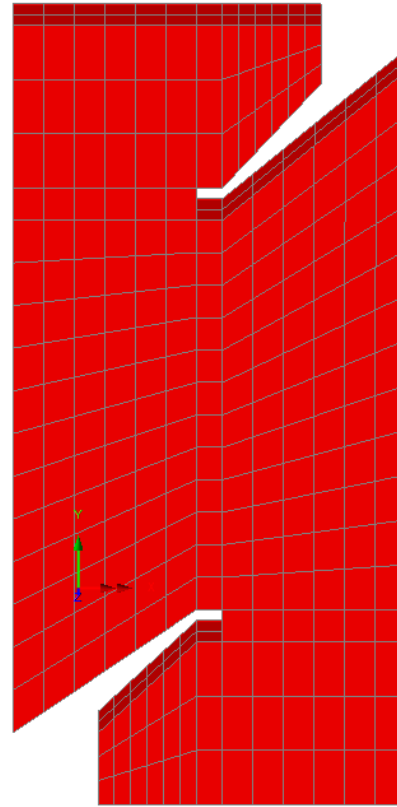
Figure 23b Finite element mesh

The experimental and numerical responses are shown in Figure 24. A deformed mesh plot showing contours of the major principal strain at the final load step is given in Figure 25. The numerical predictions lie largely between the results from two experimental tests with the same nominal opening displacement. A region where shear softening occurs before the coarse aggregate contact behaviour becomes dominant may be seen in the numerical results for both the shear and normal responses. Overall, the numerical results are considered to match the experimental data well.
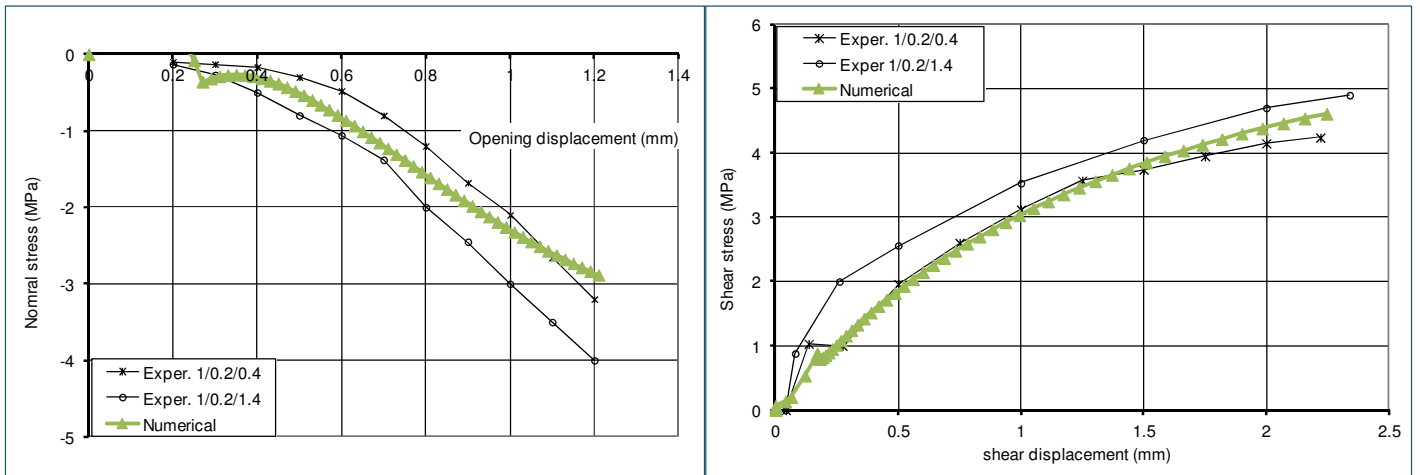
Figure 24 Experimental and numerical results.
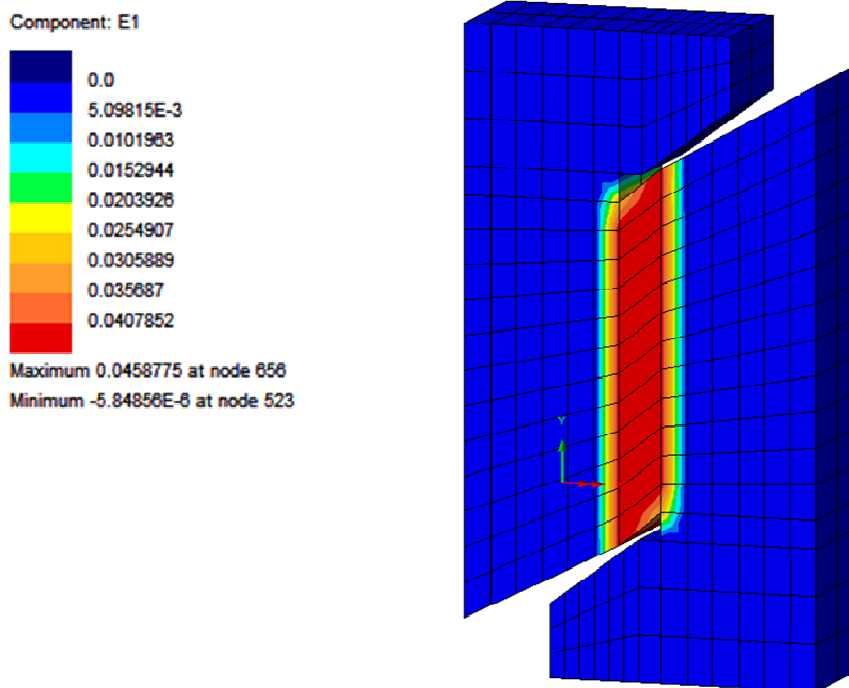


Figure 25. Deformed mesh plot showing major principal strain contours at the final load step.

### 6.3 Numerical convergence history with different degrees of closure transition.

One of the main aims of the work presented here was to develop a rough crack contact model with improved robustness relative to models in which crack closure is modelled abruptly. To explore this further, example 4 is used for a convergence study in which the effect of varying the abruptness of shear crack contact on the solution convergence history is evaluated. This abruptness is governed by the parameter $c_{zn}$ (see equation 18), which is normally fixed at a value of 9; however, it is varied here for the purpose of the present study from 5 (soft closure) to 50 (abrupt closure).

The  effect of varying this parameter on the opening-closing uniaxial response is illustrated in Figure 26. This shows the results of a plane-stress analysis using a single 50x50 mm element in which a relative displacement in the y-direction is prescribed. The material properties used, other than the $c_{zn}$ values, are identical to those used in Example 4.
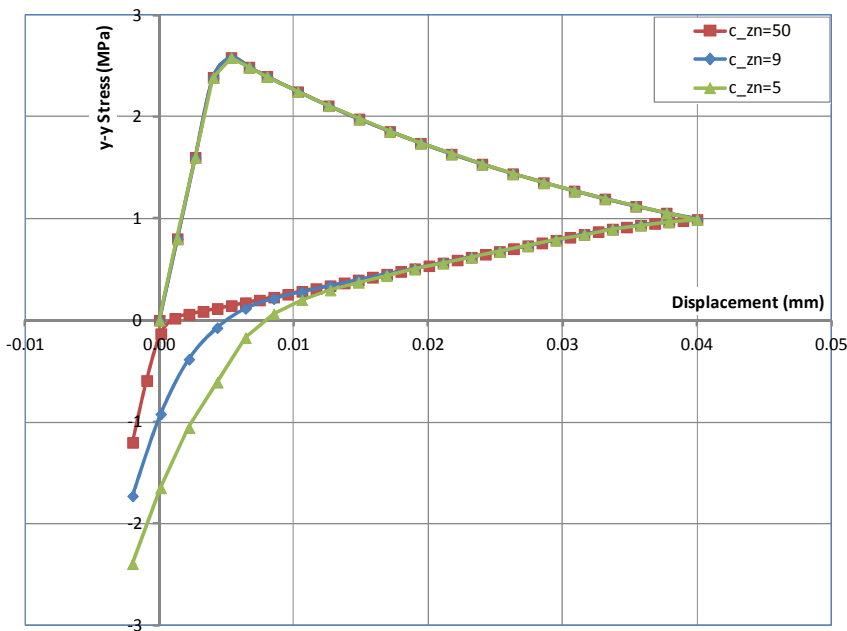


Figure 26. Direct opening - closing response curves for different closing parameters ($c_{zn}$).

The specimen in example 4 was reanalysed using the above $c_{zn}$ values. The steps requiring the greatest number of iterations to converge are those associated with the build up of shear contact. This occurs between increments  10 and 15.  The convergence history for this range of increments is presented in Table 4 for all 3 analysis cases.

It may be seen, by comparing results from the 3 cases for increments 11 and 12, that far fewer iterations are required for convergence when there is a smooth contact transition (i.e. when $c_{zn}$=5 or 9) than when abrupt crack contact is considered.

A further point relates to the tangent matrix, for which the derivation was given in Section 5.2. This gives the consistent tangent matrix for all elements in which permanent cracks have formed. Such a tangent matrix should lead to quadratic equilibrium convergence, once the out of balance error becomes sufficiently small (e.g.  $10^{-2}$) and all cracks have stabilised. The results in Table 4 suggest that this is indeed the case, since the results from the smooth contact analyses do tend towards quadratic convergence in the latter iterations of each step.

33

**Table 4. Convergence history for selected increments**

| $c_{zn}=50$ (abrupt closure) | | | $c_{zn}=9$ (standard closure) | | | $c_{zn}=5$ (soft closure) | | |
|---|---|---|---|---|---|---|---|---|
| Increment | Iter | $\psi_f$ (%) | Increment | Iter | $\psi_f$ (%) | Increment | Iter | $\psi_f$ (%) |
| 10 | 1 | 4.70E+01 | 10 | 1 | 9.46E+00 | 10 | 1 | 9.46E+00 |
| 10 | 2 | 2.35E+01 | 10 | 2 | 1.59E-01 | 10 | 2 | 1.58E-01 |
| 10 | 3 | 1.04E+01 | 10 | 3 | 4.79E-03 | 10 | 3 | 4.78E-03 |
| 10 | 4 | 4.47E+00 | | | | | | |
| 10 | 5 | 2.92E-03 | | | | | | |
| 11 | 1 | 1.13E+02 | 11 | 1 | 9.66E+01 | 11 | 1 | 9.58E+01 |
| 11 | 2 | 9.47E+01 | 11 | 2 | 8.61E+00 | 11 | 2 | 8.61E+00 |
| 11 | 3 | 1.37E+02 | 11 | 3 | 5.07E-01 | 11 | 3 | 5.09E-01 |
| 11 | 4 | 1.94E+02 | 11 | 4 | 3.03E-02 | 11 | 4 | 3.04E-02 |
| 11 | 5 | 1.85E+02 | 11 | 5 | 1.42E-04 | 11 | 5 | 1.58E-04 |
| 11 | 6 | 1.31E+02 | | | | | | |
| 11 | 7 | 2.89E+01 | | | | | | |
| 11 | 8 | 1.60E+01 | | | | | | |
| 11 | 9 | 3.14E-01 | | | | | | |
| 11 | 10 | 8.35E-04 | | | | | | |
| 12 | 1 | 1.13E+02 | 12 | 1 | 2.72E+01 | 12 | 1 | 2.45E+01 |
| 12 | 2 | 4.11E+01 | 12 | 2 | 6.74E-01 | 12 | 2 | 9.49E-01 |
| 12 | 3 | 4.23E+01 | 12 | 3 | 3.30E-02 | 12 | 3 | 4.24E-02 |
| 12 | 4 | 4.88E+01 | 12 | 4 | 1.64E-03 | 12 | 4 | 1.94E-03 |
| 12 | 5 | 1.38E+02 | | | | | | |
| 12 | 6 | 1.24E+02 | | | | | | |
| 12 | 7 | 1.28E+02 | | | | | | |
| 12 | 8 | 1.09E+02 | | | | | | |
| 12 | 9 | 1.22E+02 | | | | | | |
| 12 | 10 | 7.30E+01 | | | | | | |
| 12 | 11 | 1.43E+02 | | | | | | |
| 12 | 12 | 3.27E+00 | | | | | | |
| 12 | 13 | 1.43E+02 | | | | | | |
| 12 | 14 | 2.38E+00 | | | | | | |
| 12 | 15 | 1.26E-02 | | | | | | |
| 12 | 16 | 3.03E-05 | | | | | | |
| 13 | 1 | 2.10E+01 | 13 | 1 | 6.79E+01 | 13 | 1 | 4.16E+01 |
| 13 | 2 | 3.22E+00 | 13 | 2 | 2.42E+00 | 13 | 2 | 6.46E-01 |
| 13 | 3 | 8.25E-01 | 13 | 3 | 9.84E-02 | 13 | 3 | 2.02E-02 |
| 13 | 4 | 4.89E-01 | 13 | 4 | 4.23E-03 | 13 | 4 | 7.27E-04 |
| 13 | 5 | 1.63E-03 | | | | | | |
| 14 | 1 | 8.17E+00 | 14 | 1 | 1.40E+01 | 14 | 1 | 1.92E+01 |
| 14 | 2 | 1.26E+00 | 14 | 2 | 3.17E-01 | 14 | 2 | 3.47E-01 |
| 14 | 3 | 2.68E-01 | 14 | 3 | 1.03E-02 | 14 | 3 | 1.57E-02 |
| 14 | 4 | 7.55E-02 | 14 | 4 | 4.16E-04 | 14 | 4 | 7.01E-04 |
| 14 | 5 | 1.07E-05 | | | | | | |
| 15 | 1 | 3.57E+00 | 15 | 1 | 3.24E+00 | 15 | 1 | 2.69E+00 |
| 15 | 2 | 3.31E-01 | 15 | 2 | 1.03E-01 | 15 | 2 | 8.71E-02 |
| 15 | 3 | 8.94E-02 | 15 | 3 | 3.82E-03 | 15 | 3 | 2.99E-03 |
| 15 | 4 | 2.46E-02 | | | | | | |
| 15 | 5 | 4.19E-06 | | | | | | |

$\psi_f$ is the L2 norm of out of balance forces.

# 7. CONCLUSIONS

A model framework that uses a split between damaged and undamaged components of a representative crack-plane and simulates both direct crack closure and shear contact (aggregate interlock) with the same mechanics provides a natural basis for representing the complexities of concrete crack behaviour. A new damage-contact crack-plane model, based on this framework, is presented that is applicable to discrete cracks as well as to embedded (smeared) crack-bands in continuum finite elements.

Simulating abrupt crack closure in finite element concrete models can give rise to numerical difficulties but these can be alleviated by the introduction of a transition between open and closed crack states. Furthermore, experimental data show that real crack closure in concrete is a gradual, rather than abrupt, process. Thus, including a smooth transition between open and closed crack states in a numerical model not only enhances numerical robustness but also improves accuracy.

An effective contact surface can be derived from experimental tests on cracked concrete specimens in which cracks are formed under normal loading and subsequently loaded in shear. The effective contact surface, in relative-displacement space, has the shape of round-nosed cone, centred on the normal relative-displacement axis and is conveniently expressed as an equation with the properties of a signed-distance function. The effective contact function provides a good basis for a rough crack contact model with the crack-plane tractions being computed from the function value and the elastic stiffnesses of a representative band of material.

Experimental data show that both the shear stiffness and maximum shear stress developed across a crack-band loaded in shear reduce with increasing crack opening. This behaviour is therefore included in the numerical crack model presented.

When a crack-plane model is adapted for continuum elements it is necessary not only to scale the normal stress–strain damage evolution function, as in the crack-band model, but also to scale the contact reduction function. This important issue has been overlooked in previous work by the authors and by others.

A new form for the consistent tangent matrix and associated stress recovery procedure (from that of Reference [16]) is required due to the introduction of the smoothed contact transition functions into the crack-plane model.

The new model is able to represent a range of characteristic concrete cracking behaviour exhibited in experimental tests including;
- Mode 1 and mixed mode crack formation and evolution;
- Unloading and reloading behaviour under normal loading, including a gradual transition between open and closed crack states;
- An increasing crack closure transition zone with increasing crack opening displacement;
- Shear contact behaviour, or aggregate interlock, when open cracks are loaded in shear.

## REFERENCES

| | |
|---|---|
| 1 | La Borderie C, Mazars J, Pijaudier-Cabot G. Response of plain and reinforced concrete structures under cyclic loadings. *American Concrete Institute* 1994; **134**:147–172. |
| 2 | Lee J, Fenves GL. Plastic-damage model for cyclic loading of concrete structures. *ASCE Journal of Engineering Mechanics* 1998; **124**:892–900. |
| 3 | Cervera M, Oliver J, Manzoli O. WA rate-dependent isotropic damage model for the seismic analysis of concrete dams. Earthquake Engineering and Structural Dynamics 1996; **25**:987–1010. |
| 4 | Rots J, de Borst R. Analysis of mixed mode fracture in concrete. *ASCE Journal of Engineering Mechanics* 1987; **113**(11), 1739–1758. |
| 5 | ACI-ASCE Committee 426. The shear strength of reinforced concrete members. *Journal of the Structural Division* 1973; **99**(6) |
| 6 | Paulay T, Loeber PJ. Shear transfer by aggregate interlock. In *Shear in Reinforced Concrete*, Publication SP-42, American Concrete Institute 1974, 1-15. |
| 7 | Bažant ZP, Oh BH. Crack band theory for fracture in concrete. *Materials and Structures* 1983, **16**: 155–177. |
| 8 | Crisfield MA. Difficulties with current numerical models for reinforced concrete and some tentative solutions. In Damjanic F, Hinton E, Owen DRJ, Bicanic N, Simovic V (eds), International Conference on Computer-Aided Analysis and Design of Concrete Structures, Pineridge Press, Swansea, 1984, 331–358. |
| 9 | Feenstra PH, de Borst R. A plasticity model and algorithm for mode-I cracking in concrete. *International Journal for Numerical Methods in Engineering* 1995*;* **38**: 2509–2529. |
| 10 | Rots JG. *Computational modeling of concrete fracture*. PhD Thesis, Delft University of Technology, The Netherlands. 1988 |
| 11 | Rots JG, Invernizzi S. Regularized sequentially linear saw-tooth softening model. *International Journal for Numerical and Analytical Methods in Geomechanics incorporating Mechanics of Cohesive-Frictional Materials* 2004; **28**, 821–856. |
| 12 | Oliver J, Husepe AE, Blanco S, Linero DL. Stability and robustness issues in numerical modelling of material failure with the strong discontinuity approach. *Computer Methods in Applied Mechanics and Engineering* 2006; **195**: 7093–7114. |
| 13 | de Borst R, Crisfield MA, Remmers JJC, Verhoosel CV. Non-linear finite element analysis of solids and structures. Wiley: Chichester, 2012. |
| 14 | Feenstra PH, de Borst R, Rots JG. Numerical study on crack dilatancy. I: Models and stability analysis. *ASCE Journal of Engineering Mechanics* 1991; **117**(4): 733–753. |
| 15 | Richard B, Ragueneau F, Cremona C, Adelaide L. Isotropic continuum damage mechanics for concrete under cyclic loading: stiffness recovery, inelastic strains and frictional sliding. *Engineering Fracture Mechanics* 2010; **77**:1203–1223. |
| 16 | Jefferson AD. Craft - a plastic-damage-contact model for concrete. I. Model theory and thermodynamic considerations, *International Journal of Solids and Structures* 2003; **40**(22): 5973–5999. |
| 17 | Hofbeck J.A, Ibrahim IO, Mattock, MH. Shear transfer in reinforced concrete. *American Concrete Institute Journal* 1969; 66(2): 119–128. |
| 18 | Mattock AH, Hawkins NM. Shear transfer in reinforced concrete recent research, *Precast/Prestressed Concrete Institute Journal* 1972, 17(2): 55–75. |
| 19 | Walraven JC, Reinhardt HW. Theory and experiments on the mechanical behavior of cracks in plain and reinforced concrete subjected to shear loading. *Heron* 1981; **26**(1A), Delft, The Netherlands. |
| 20 | Nooru-Mohamed M.B. *Mixed-mode fracture of concrete: an experimental approach*. PhD Thesis, Delft University of Technology, The Netherlands, 1992. |
| 21 | Hassanzadeh M. *Behaviour of fracture process zones in concrete influenced by simultaneously applied normal and shear displacements*. PhD Thesis, Lund Institute of Technology, Sweden, 1991. |
| 22 | Walter R, Olesen JF. Cohesive mixed mode fracture modelling and experiments. *Engineering Fracture Mechanics* 2008; **75**(18):5163–5176. |

| 23 | Jacobsen JS, Poulsen PN, Olesen JF. Characterization of mixed mode crack opening in concrete. *Materials and Structures* 2012; **45**: 107–122. |
| 24 | Li B, Maekawa K, Okamura H. Contact density model for stress transfer across cracks in concrete. *Journal of the Faculty of Engineering*, the University of Tokyo 1989; **40**(1): 9–52. |
| 25 | Boussa H, Tognazzi-Lawrence C, La Borderie C. A model for computation of leakage through damaged concrete structures. *Cement and Concrete Composites* 2001; **23**:279–287. |
| 26 | Jacobsen JS, Poulsen PN, Olesen JF, Krabbenhoft K. Constitutive mixed mode model for cracks in concrete. *Engineering Fracture Mechanics* 2013; **99**: 30–47. |
| 27 | Reinhardt HW. Fracture mechanics of an elastic softening material like concrete. *Heron* 1984; **29**(2): 1–42, Delft, The Netherlands. |
| 28 | ASCE Task Committee on Finite Element Analysis of Reinforced Concrete Structures. Finite element analysis of reinforced concrete structures, 1982, ASCE. |
| 29 | Owen DRJ, Figueiras JA, Damjanic F. Finite element analysis of reinforced and prestressed concrete structures including thermal loading. *Computer Methods in Applied Mechanics and Engineering* 1983; **41**: 323–366. |
| 30 | de Borst R, Nauta P. 1985. Non-Orthogonal cracks in a smeared finite element model. *Engineering Computations* 1985; **2**: 35–46. |
| 31 | de Borst R. Fracture in quasi-brittle materials: a review of continuum damage-based approaches. *Engineering Fracture Mechanics* 2002; **69**: 95–112. |
| 32 | Slobbe AT, Hendriks MAN, Rots JG. Sequentially linear analysis of shear critical reinforced concrete beams without shear reinforcement. *Finite Elements in Analysis and Design* 2012; **50**: 108–124. |
| 33 | Hansen NR, Schreyer HL. 1995. Damage deactivation. *ASME Journal of Applied Mechanics* 1995; **62**: 450–458. |
| 34 | Mazars J, Pijaudier-Cabot G. Continuum damage theory-application to concrete. ASCE *Journal of Engineering Mechanics* 1989; 115(2): 345–365. |
| 35 | Carol I, Willam K. Spurious energies dissipation/generation in stiffness recovery models for elastic degradation and damage. *International Journal of Solids and Structures* 1996; **33** (20–22): 2939–2957. |
| 36 | Wu J-Y, Xu S-L. Reconsideration on the elastic damage/degradation theory for the modeling of microcrack closure-reopening (MCR) effects. *International Journal of Solids and Structures* 2013; **50**: 795–805. |
| 37 | Mazars J, Berthaud Y, Ramtani S. The unilateral behaviour of damaged concrete. *Engineering Fracture Mechanics* 1990; **35**: 629–635. |
| 38 | Comi C, Perego U. Fracture energy based bi-dissipative damage model for concrete. *International Journal of Solids and Structures* 2001; **38**: 6427–6454. |
| 39 | Richard B, Ragueneau F. Continuum damage mechanics based model for quasi brittle materials subjected to cyclic loadings: Formulation, numerical implementation and applications. *Engineering Fracture Mechanics* 2013; **98**: 383–406. |
| 40 | Bazant ZP, Gambarova P. Rough cracks in reinforced concrete. Journal of the Structural Division, *Proceedings of the ASCE* 1980; **106**(4): 819–842. |
| 41 | Divakar MP, Fafitis A, Shah SP. Constitutive model for shear transfer in cracked concrete. ASCE *Journal of Structural Engineering* 1987; **113**(5): 1046–1062. |
| 42 | Haberfield CM, Johnston IW. A mechanistically-based model for rough crack joints. *International Journal of Rock Mechanics Mining Sciences & Geomechanics Abstracts* 1994; **31**(4): 279–292. |
| 43 | Ali MA, White RN. Enhanced contact model for shear friction of normal and high strength concrete. *American Concrete Institute Structural Journal* 1999; **96**(3): 348–360. |
| 44 | Jefferson AD. A constitutive model for aggregate interlock on formed crack planes. *International Journal of Numerical and Analytical Methods in Geomechanics* 2002, **26**: 1–21. |
| 45 | Alfano G, Sacco E. Combining interface damage and friction in a cohesive-zone model. *International Journal for Numerical Methods in Engineering* 2006; **68**(5): 542–582. |

| 46 | Mihai IC, Jefferson AD. A multi-asperity plastic-contact crack plane model for geomaterials. *International Journal of Numerical and Analytical Methods in Geomechanics* 2013; **37**:1492–1509. |
| 47 | Carol I, Prat PC, López CM. A normal-shear cracking model. Application to discrete crack analysis. ASCE *Journal of Engineering Mechanics* 1997; **123**: 765–773. |
| 48 | Lopez CM, Carol I, Aguado A. Meso-structural study of concrete fracture using interface elements. *Materials and Structures* 2008; **41**: 583–599. |
| 49 | Lens LN, Bittencourt E, d'Avila VMR. Constitutive models for cohesive zones in mixed-mode fracture of plain concrete. *Engineering Fracture Mechanics* 2009; **76**:2281–2297. |
| 50 | Snozzi L, Molinari J-F. A cohesive element model for mixed mode loading with frictional contact capability. *International Journal for Numerical Methods in Engineering* 2013; **93**:510–526. |
| 51 | Hillerborg M, Modeer M, Peterson P. Analysis of crack formation and crack growth in concrete by means of fracture mechanics and finite elements. *Cement and Concrete Research* 1976; **6**: 773–782. |
| 52 | Jirasek M, Bauer M. Numerical aspects of the crack band approach. *Computers and Structures* 2012; **110–111**: 60–78. |
| 53 | Theiner Y, Hofstetter G.  Numerical prediction of crack propagation and crack widths in concrete structures *Engineering Structures* 2009; **31**: 1832–1840. |
| 54 | Oliver J, Husepe AE, Samaniego E. A study on finite elements for capturing strong discontinuities. *International Journal for Numerical Methods in Engineering* 2003; **56**: 2135–2161. |
| 55 | Dujc J, Brank B, Ibrahimbegovic A. Stress-hybrid quadrilateral finite element with embedded strong discontinuity for failure analysis of plane stress solids. *International Journal for Numerical Methods in Engineering* 2013; **94**:1075–1098. |
| 56 | Belytschko T, Black T. Elastic crack growth in finite elements with minimal remeshing. *International Journal for Numerical Methods in Engineering* 1999; **45**(5):601–620. |
| 57 | Remmers JJC,  de Borst R, Needleman A. A cohesive segments method for the simulation of crack growth. *Computational Mechanics* 2003; 31: 69–77. |
| 58 | Fries T-P, Belytschko T. The extended/generalized finite element method: An overview of the method and its applications. *International Journal for Numerical Methods in Engineering* 2010; **84**(3): 253–304. |
| 59 | Mosler J, Meschke G. Embedded crack vs. smeared crack models: a comparison of elementwise discontinuous crack path approaches with emphasis on mesh bias. *Computer Methods in Applied Mechanics and Engineering* 2004; **193**(30–32): 3351–3375. |
| 60 | Sellier A, Casaux-Ginestet G, Buffo-Lacarrière L, Bourbon X. Orthotropic damage coupled with localised crack reclosure processing. Part I: Constitutive laws. *Engineering Fracture Mechanics* 2013, **978**:148–167. |
| 61 | Jefferson AD.  Plastic-damage model for interfaces in cementitious materials. *ASCE Journal of Engineering Mechanics* 1998; **124**(7): 775–782. |
| 62 | Ragueneau F, La Borderie C, Mazars J. Damage model for concrete-like materials coupling cracking and friction, contribution towards structural damping: first uniaxial applications. *Mechanics of Cohesive-Frictional Materials* 2000; **5**: 607–626. |
| 63 | Crisfield MA. *Non-linear Finite Element Analysis of Solids and Structures* Vols1 & 2. Wiley: Chichester, 1991. |
| 64 | Wriggers, P.  Computational Contact Mechanics, 2nd edition, 2006. Springer, Berlin |
| 65 | Oliver J. A consistent characteristic length for smeared cracking models. *Int J Numer Methods Eng* 1989;28:461–74. |
| 66 | LUSAS (2014). www.lusas.com |

## Acknowledgements

## APPENDICES

### A. TRANFORMATION MATRIX

The transformation matrix which gives the relationship between the crack-plane stresses and Cartesian stresses in reduced vector form is given by:

$$\mathbf{N} = \begin{bmatrix} r_{1_1}^{\ 2} & r_{1_2}^{\ 2} & r_{1_3}^{\ 2} & 2r_{1_1}r_{1_2} & 2r_{1_2}r_{1_3} & 2r_{1_1}r_{1_3} \\ r_{1_1}r_{2_1} & r_{1_2}r_{2_2} & r_{1_3}r_{2_3} & r_{1_2}r_{2_1}+r_{1_1}r_{2_2} & r_{1_3}r_{2_2}+r_{1_2}r_{2_3} & r_{1_1}r_{2_3}+r_{1_3}r_{2_1} \\ r_{1_1}r_{3_1} & r_{1_2}r_{3_2} & r_{1_3}r_{3_3} & r_{1_2}r_{3_1}+r_{1_1}r_{3_2} & r_{1_3}r_{3_2}+r_{1_2}r_{3_3} & r_{1_1}r_{3_3}+r_{1_3}r_{3_1} \end{bmatrix}$$
(A1)

which is derived from the tensor transformation $\tilde{\sigma}_{ij} = r_{i_k}r_{j_l}\sigma_{kl}$

### B. DERIVATION OF CONTACT TRANSITION FUNCTION

The aim is to derive a function which gives a smooth transition across a crack closure point. The equations are developed in terms of the one-dimensional damage-contact model illustrated in Figure B1. The model without a smooth transition is represented by equation (B1) in which the stress ($\sigma$), relative displacement ($u$), stiffness ($k$) and damage parameter ($\omega \in [0,1]$) are all scalars.

$$\sigma = (1-\omega)ku + \omega H(u)\,ku = \left[k_u + H(u)k_c\right]u$$
(B1)

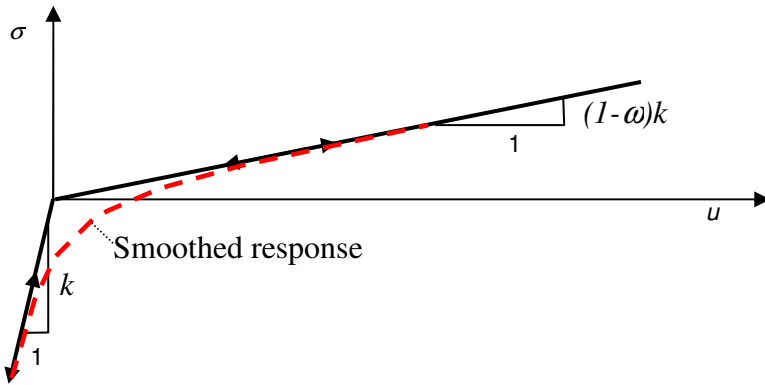where the Heaviside function $H$(u) =1 $\forall$ u$\leq$0  &  =0 $\forall$ u>0        .



Figure B1. Standard and smoothed damage-contact response

A function which gives a smooth transition in the gradient $k_T$ ( where $k_T = \dfrac{d\sigma}{du}$) of (B1) is as follows:

$$k_T(u) = k_u + k_c\left(\frac{1 - tanh\left(u/u_z\right)}{2}\right)$$
(B2)

in which the parameter $u_z$ governs the size of the transition zone in $u$.

An expression for a smoothed stress response may now be derived from the integral of this expression:

$$\sigma(u) = \int k_T(u)\,du = k_u u + \frac{k_c}{2}\left( (u - u_{lm}) - u_z \cdot \left[ \ln\left( \cosh\left( \frac{u}{u_z} \right) \right) - \ln\left( \cosh\left( \frac{u_{lm}}{u_z} \right) \right) \right] \right)$$

(B3)

in which $u_{lm}$ is a constant, the value of which is determined below. The choice of integration constant is made to allow control over the region to which the transition is applied.

As $u \rightarrow \infty$ $\sigma(u) \rightarrow k_u u$ and therefore $\left\{ (u - u_{lm}) - u_z \cdot \left[ \ln\left( \cosh\left( \frac{u}{u_z} \right) \right) - \ln\left( \cosh\left( \frac{u_{lm}}{u_z} \right) \right) \right] \right\} \rightarrow 0$

(B4)

It is noted that

$$\lim_{u \to \infty} \left( u - u_z \cdot \ln\left( \cosh\left( \frac{u}{u_z} \right) \right) \right) = u_z \ln(2)$$

.

(B5)

Therefore, $u_{lm}$ may be determined from the following equation, which is only satisfied at $u_{lm} = \infty$

$$\frac{u_{lm}}{u_z} - \ln\left( \cosh\left( \frac{u_{lm}}{u_z} \right) \right) = \ln(2)$$

.

(B6)

However, the error is $O(e^{-2\frac{u_{lm}}{u_z}})$ for $u_{lm}/u_z > 2$, hence the value $u_{lm}/u_z = m_{lm} = 7$ gives acceptable accuracy.

Thus, the transition function with limits to avoid a zero divide and yet which limits the error to $O(e^{-14})$ is:

$$\lambda(u) = \frac{1}{2}\left[ 1 - \frac{u}{u - u_{lm}} \ln\left( \frac{\cosh\left( u/u_z \right)}{\cosh(m_{lm})} \right) \right] \qquad \forall \left| u/u_z \right| \le m_{lm}$$

$$= \frac{1}{2}\left[ 1 - \frac{u}{u - u_{lm}} \left( \left( \frac{\frac{u}{u_z}}{\left| \frac{u}{u_z} \right|} \right) \frac{u}{u_z} + \ln\left( \frac{1}{2\cosh(m_{lm})} \right) \right) \right] \qquad \forall \left| u/u_z \right| > m_{lm}$$

(B7)

noting that $ln(a)-ln(b)=ln(a/b)$ and $\lim_{a \to \infty}\left( \frac{\cosh a}{\cosh m} - \left( a + \ln\left( \frac{1}{2\cosh(m)} \right) \right) \right) \rightarrow 0$ .

Using the above transition function in equation (B1) gives the following continuous function with a smooth response:

$$\sigma = (1-\omega)ku + \omega\lambda(u)\,k\,(u - u_{lm})$$

(B8)

## C. SHEAR CONTACT FUNCTION SCALING WITH ELEMENT SIZE.

Assuming that the shear stiffness across a physical fracture process zone of width $h$ is factored by the contact reduction function $H(\tilde{u}_1)$, then the shear stress across this zone of material with shear modulus $G$, in terms of the shear displacement ($\tilde{u}_2$), is:

$$\tilde{\sigma}_{12} = H(\tilde{u}_1)\frac{G}{h}\tilde{u}_2 \tag{C1}$$

Noting that the inelastic component of $\tilde{u}_2$ is denoted $\breve{u}_2$, (C1) may be written:

$$\tilde{\sigma}_{12} = \frac{G}{h}(\tilde{u}_2 - \breve{u}_2) \tag{C2}$$

Equating (C1) to (C2), dropping all dependencies for clarity, and rearranging gives:

$$\tilde{u}_2 = \frac{\breve{u}_2}{(1-H)} \tag{C3}$$

Using (C3) in (C1) and rearranging gives the following equation for the inelastic crack sliding displacement:

$$\breve{u}_2 = \frac{(1-H)}{H}\frac{\tilde{\sigma}_{12}h}{G} \tag{C4}$$

In a linear element of characteristic length $\ell_{ch}$ with constant shear strain $\tilde{\varepsilon}_{12}$ and inelastic strain $\breve{\varepsilon}_{12} = \breve{u}_2/\ell_{ch}$, the associated shear stress is given by:

$$\tilde{\sigma}_{12} = G\left(\tilde{\varepsilon}_{12} - \frac{\breve{u}}{\ell_{ch}}\right) \tag{C5}$$

Substituting for $\breve{u}_2$ from (C4) into (C5) gives:

$$\tilde{\sigma}_{12} = G\left(\tilde{\varepsilon}_{12} - \frac{(1-H)\tilde{\sigma}_{12}h}{HG\ell_{ch}}\right) \tag{C6}$$

Rearranging gives:

$$\tilde{\sigma}_{12} = H_c G\tilde{\varepsilon}_{12} \tag{C7}$$

in which the continuum form of the contact reduction function is given by:

$$H_c = \frac{H\ell_{ch}}{H\ell_{ch} + (1-H)h} \tag{C8}$$

## D. DAMAGE FUNCTION

The crack-plane damage function $\phi_{\rm d}(\tilde{\varepsilon},\zeta)$ is asymptotic to an equivalent strain friction surface and is orthogonal to the normal strain axis at its intercept with that axis, as illustrated in Figure D1.

$$\phi_{\rm d}(\tilde{\varepsilon},\zeta) \;=\; \frac{\tilde{\varepsilon}_{11}}{2}\left[1+\left(\frac{\mu_\varepsilon}{{\rm r}_\zeta}\right)^2\right]+\frac{1}{2{\rm r}_\zeta^{\,2}}\sqrt{\left({\rm r}_\zeta^{\,2}-\mu_\varepsilon^{\,2}\right)^2\tilde{\varepsilon}_{11}^{\,2}+4{\rm r}_\zeta^{\,2}\left(\tilde{\varepsilon}_{12}^{\,2}+\tilde{\varepsilon}_{13}^{\,2}\right)}-\zeta \tag{D1}$$

Or

$$=\zeta_{\rm eq}(\tilde{\varepsilon})-\zeta \tag{D2}$$

The constants $r_\zeta$ and $\mu_\varepsilon$ are the relative shear strain intercept and the asymptotic shear friction factor respectively. However, these are not the primary material constants used in model; rather, the more familiar and available stress counterparts of these parameters are used (See section 5.4). These are the relative shear stress intercept $r_\sigma$ and the asymptotic friction factor μ, the former of which is defined as follows:

$$r_\sigma = c/f_t \tag{D3}$$

where $c$ is basic crack interface shear strength.

The strain based damage parameters are then computed from the following equations:

$$\mu_\varepsilon = \mu\cdot\frac{E}{G}$$

$$\phantom{xxxxxxxxxxxxxxxxxxxxxxxxxxxxxxxxxxxxxxx} \tag{D4a,b}$$
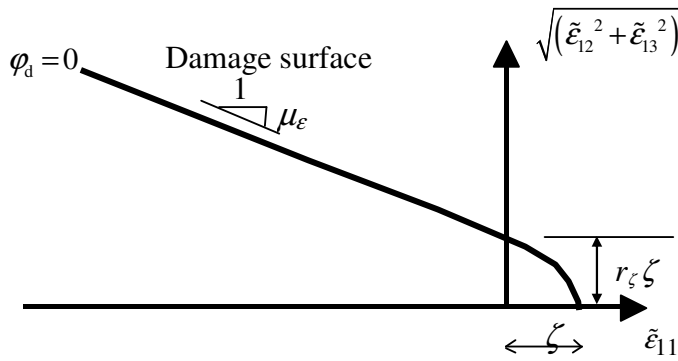
$${\rm r}_\zeta = {\rm r}_\sigma\cdot\frac{E}{G}$$



Figure D1. Damage function in local strain space